2019

Metallized printed microstructures for precision biomedical recording and stimulation

https://hdl.handle.net/2144/36047

Boston University

BOSTON UNIVERSITY

COLLEGE OF ENGINEERING

Thesis

METALLIZED PRINTED MICROSTRUCTURES FOR PRECISION

BIOMEDICAL RECORDING AND STIMULATION

by

JEREMY ROBERT GLEICK

B.S., University of California Los Angeles, 2014

Submitted in partial fulfillment of the

requirements for the degree of

Master of Science

2019

Approved by

First Reader   _____
Timothy M. Otchy, Ph.D.
Research Assistant Professor of Biology

Second Reader   _____
Timothy J. Gardner, Ph.D.
Associate Professor of Biology
Associate Professor of Biomedical Engineering

Third Reader   _____
Xue Han, Ph.D.
Associate Professor of Biomedical Engineering

Fourth Reader   _____
David Boas, Ph.D.
Professor of Biomedical Engineering
Professor of Electrical and Computer Engineering

Acknowledgments

I'd like to thank Dr. Tim Otchy and Dr. Tim Gardner for welcoming me into the lab and offering the opportunities to find and develop this project. Thanks especially to Tim O. for being receptive and open to my endless dropping in with updates, questions, and ideas, and to Tim Gardner for his enthusiasm about the project's potential and the many suggestions of new paths to investigate.

I would like to thank Dr. Xue Han for her valuable feedback on the project and how to focus correctly on its real values, and both Dr. Han and Dr. David Boas for their teaching in my courses.

Thanks of course to the rest of the Otchy/Gardner lab for their support and feedback throughout the process, especially Dan Leman for his upbeat presence and direct help with the characterization setup and Ellen Witkowski in the Davison lab for her especially thorough feedback for my defense presentation.

Thanks lastly to my parents for far too many things to enumerate, to Khy and Derek Labri for a haven to escape to, and to Jay Dragon, Devon Brinner, Sidus Chayes, Maya Ziv, Jessica Loginov, and Worsey for holding the universe together.

METALLIZED PRINTED MICROSTRUCTURES FOR PRECISION

BIOMEDICAL RECORDING AND STIMULATION

JEREMY ROBERT GLEICK

ABSTRACT

Implantable electrodes are the central tool for many techniques and treatments in biomedical research and medicine. There is a trend in these tools towards arrays of tissue-penetrating microelectrodes with low geometric surface areas for purposes of both increasing the specificity of recording/stimulation and reducing tissue damage due to insertion trauma and reactive immune responses. However, smaller electrode sizes present new constraints – both difficulty in fabrication as well as significant limitations on effective charge storage/injection capacities as well as higher impedances, making smaller electrodes less capable of easily passing charge safely and efficiently.

Fabricating structures on the scale of tens of microns and below poses significant challenges compared to well established machining at larger sizes. Established sets of techniques such as classic MEMS processes are limited to relatively specific shapes, with significant limitations in their ability to produce curved surfaces and surfaces which are not composed of highly distinct stepped layers.

We developed a method for improvement of impedance and charge storage capacity of flat electrodes without affecting geometric surface area (footprint) using Resonant Direct Laser Writing (rDLW) 3D printing to fabricate

high surface area 3D structures, which were then rendered conductive.

The ability to perform DLW printing at a range of laser powers on opaque reflective surfaces is demonstrated, previously a known limitation of direct laser writing. This is demonstrated through a variety of example prints. This capability opens the door to many new possibilities in micron resolution polymer printing which were previously inaccessible, with potentially far reaching ramifications for microfabrication.

Table of Contents

List of Tables

List of Figures

1 Background

1.1 Electrodes in Medicine

Modern stimulating electrodes are used in an enormous variety of applications in modern medicine, in both recording and stimulating capacities (Li and Mogul 2007; Amon and Alesch 2017; Clark 2006; Brownlee 1992; Rijkhoff et al. 1994). Many parts of the body produce a measurable electrical signal such as the brain and spinal cord, peripheral nerves, heart tissue, and muscles, and many more present electrically measurable properties such as the electrodermal response of the skin, or skin conductance (Lykken and Venables 1971; Mirvis and Goldberger 2001; Frank and Fuortes 1955). Modulation of the body through electrical currents is similarly common in medicine, either directly through application of an electrode as in the case of nerve stimulation by a modern prosthesis or indirectly through use of magnetic fields such as during transcranial magnetic stimulation (Hallett 2000; Veraart et al. 2003; Gandiga et al. 2006).

An electrode is any component intended to bridge the gap between a fabricated, generally metal circuit and a nonmetal component such as biological tissue. While the contact surfaces of an electrode may be composed of metal, many other conductive materials are commonly used including conductive polymers or sponges soaked with conductive liquid (Cogan 2008; Green et al. 2008; Geddes and Roeder 2003). Commonly used electrodes may be as large as several inches across, as in the case of defibrillator or ECG equipment (Dalzell et al. 1989). When dealing with electrodes applied to the body larger is

often better: a high amount of charge applied over a small area can cause electrical burns, where the same charge distributed over a large area will not (Pearce et al. 1983).

Implantable electrodes bring this requirement to a new degree of importance. As invasive devices, implantable electrodes are necessarily very small to minimize damage during implantation procedures (Salatino et al. 2017; Biran et al. 2005). However, these small electrode sizes present new challenges. For recording electrodes, smaller devices have a harder time picking up signal over noise due to the thermal noise introduced by the impedance of the electrical interface (Lempka et al. 2006). In the case of stimulating electrodes, the delivery of sufficient charge to depolarize targeted tissues without damage becomes difficult at smaller sizes. Studies on variation in size (Harris et al. 2018) and shape (Cogan et al. 2014) show that smaller electrodes require a higher charge density to achieve the same level of stimulation, requiring increases in voltage that introduce risks of tissue and electrode damage from hydrolysis (Cogan et al. 2005). This is due to reduction in size reducing the total charge available: excitable tissue requires a sufficiently high total charge to produce a response, and under certain stimulation patterns this is difficult to achieve with small electrodes at low voltages (Merrill et al. 2005).

Given this limitation, there is a fairly narrow band of usability in major therapeutic stimulating devices wherein a device is large enough to reliably deliver the required stimulation while avoiding tissue damage on chronic use
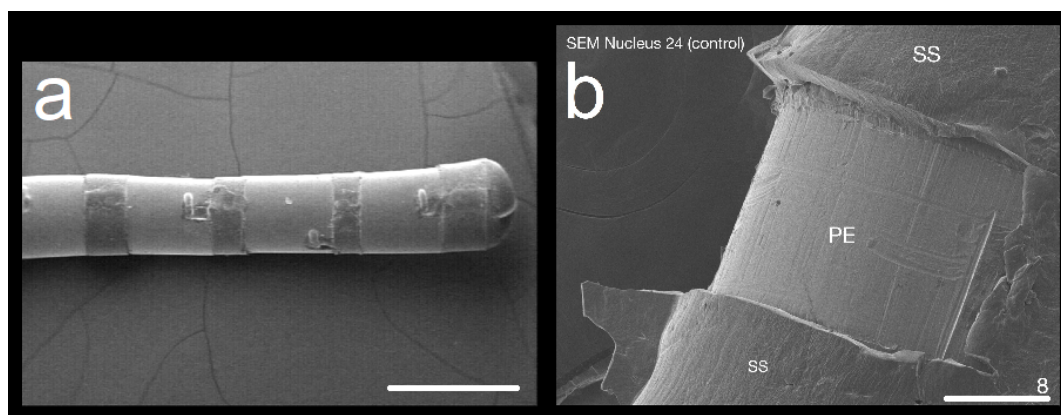
Figure 1 Scanning Electron Microscope figures of **a)** Medtronic quadripolar model 3387 (Medtronic Inc.) Deep Brain Stimulator lead, scale bar 2mm (Moss et al. 2004) and **b)** Individual electrode from Nucleus 24 cochlear electrode array, scale bar 100 µm (Nadol et al. 2014).

timescales. Commonly used medical implants in humans including Cochlear Implants (Clark 2006), Pacemakers (Brownlee 1992), Deep Brain Stimulation implants (Amon and Alesch 2017), and peripheral nerve implants for bladder control (Rijkhoff et al. 1994) all often have electrode contacts on the order of 0.5–3 mm in diameter (Figure 1). Electrodes used for stimulation in research however may be much smaller, with microwire electrodes as an example presenting contact diameters which can be 30 µm or less (Mushahwar et al. 2000).

Recording devices such as electrocorticography (ECoG) electrodes, placed beneath the skull and dura but remaining on the surface of the brain, often have similar millimeter-range diameters though they may feature as many as 250 independent contact sites (Pistohl et al. 2008; Rubehn et al. 2009). Recording electrodes planted into the brain itself are more commonly found in the context of laboratory research than in clinical use such as the use of the Utah

Array for experimental neuroprosthetics, which features 100 shanks with

electrode tips with a 36 μm diameter, narrowing towards a point (Brumberg et al.

2010). Other recording electrodes used in research contexts such as carbon

fiber microwire electrodes may even have diameters as small as 9 μm (Patel et

al. 2015). However, the challenges of reducing size while maintaining safety and

efficacy have long made difficult the translation of this research into use as major

medical devices.

1.2 Properties of Electrodes

Recording of neuronal activity is performed through electrode contacts by

identifying extracellular potentials generated by the activity of single or

ensembles of neurons or other electrically active tissue. The primary measure of

effectiveness in recording is impedance, which indicates how much of a signal

can be picked up and passed through the electrode (Cogan 2008). Electrical

stimulation of tissue occurs when cell membranes are depolarized by the

application of voltage to produce current flow between electrodes. In excitable

tissue this depolarization can induce a functional response such as neuronal

action potentials. The amount of charge that an electrode is capable of

delivering safely is termed its Charge Storage Capacity (CSC) (Elgrishi et al.

2017).

Impedance is a fundamental property of alternating current electrical

circuits, the analogue of resistance in a DC circuit, which indicates the resistance

to a current for a given voltage. This is measured through application of either a

sinusoidal voltage or current and measurement of the other property, the two of which can then be compared to calculate the impedance. Impedance of a given system will have different values for different frequencies, and while a range of frequencies is often measured, specific values are usually reported at 1 kHz for standard comparisons between devices (Cogan 2008). When membrane potentials change during cellular activity the resulting flow of ions results in polarization or depolarization of nearby electrode surfaces which is detectable as a current or voltage change. A primary challenge to the effectiveness of this recording in picking up signals over thermal noise caused by high electrode impedance (Lempka et al. 2006). As such, reducing impedance is a driving requirement in the design of better recording electrodes. Impedance is highly dependent on material choice, as different materials are more or less resistive to current flow (Geddes and Roeder 2003). Because changes in potential are detected through current shifts across the electrode surface, impedance is also heavily dependent on the surface area of the electrode (Cogan et al. 2014; Geddes and Roeder 2003).

Charge Storage Capacity (CSC) is a measurement of charge that can be delivered by an electrode for a given set of parameters including voltage range and sweep rate. In implantable electrodes, the most important of these parameters is the "water window", a voltage range typically taken as -0.6 V to 0.8 V (Cogan 2008; Beebe and Rose 1988). At voltages outside of this safe stimulation threshold, water hydrolysis begins to occur, breaking water down into

hydrogen and oxygen gas, an event which can cause damage to both the tissue and the electrode (Beebe and Rose 1988). As the voltage is adjusted back and forth between these two voltage limits at a selected speed, current is measured. Using the known sweep speed to convert voltage information to time, the area within the CV curve reveals the amount of charge that can be safely delivered by the electrode to the tissue in one cycle. Values are generally reported as cathodal CSC by taking only the negative component of current flow, though both the cathode and anode phase of a voltage sweep can be measured. As a higher surface area will result in a larger surface for current to flow across, area is highly correlated with CSC (Cogan et al. 2014). Charge transfer is also highly dependent on material, as different materials provide entirely different mechanisms of charge transfer or combinations thereof (Cogan 2008; Geddes and Roeder 2003).

When charge is delivered across an electrode, stimulation of tissue occurs via two main mechanisms: Capacitive and faradaic charge transfer (Figure 2). In capacitive charge transfer, the applied current results in the formation of a charged double layer at the surface of the electrode. As charged ions are moved from their positions in the tissue towards the electrode and vice versa polarization of the tissue is produced. Faradaic charge transfer occurs when oxidation-reduction reactions occur at the electrode surface, producing strong stimulation but generating new chemical species such as soluble metal complexes that may result in electrode degradation and potentially damaging pH

changes if charge waveforms are not balanced appropriately (Robblee et al. 1983; Merrill et al. 2005). While capacitive charge transfer is generally possible in any conductive material, faradaic charge transfer in implantable electrodes is limited in safe use to materials capable of undergoing a reversible oxidation-reduction reaction without producing dangerous byproducts. Capacitive transfer is often desirable as it does not produce any new chemical species as a result of electron transfers, however when faradaic methods are present as well a higher stimulating capacity may be possible (Weiland et al. 2002).
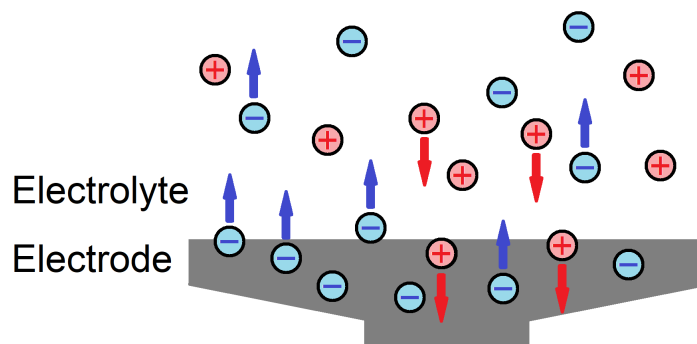
Figure 2 Illustration of capacitive and faradaic charge transfer mechanisms.

Both of these properties change as function of surface area, however there are two different definitions of surface area applicable to electrodes. Geometric surface area (GSA), also called footprint, is the area calculated assuming the electrode is entirely flat and smooth with no raised surfaces or roughness increasing its surface area. Real surface area (RSA) is the total surface area of the electrode taking into account things such as roughness or raised conductive structures on the electrode surface, and is usually more representative of actual impedance and charge storage capacity. If an electrode were flat and perfectly smooth, the GSA and RSA would be identical. If an electrode surface is rough with many hills and valleys it will have a higher RSA than GSA.

Electrode shape also has many effects on electrode efficacy (Cogan et al. 2014; Joye et al. 2009). This is visible most directly from the fact that a shape with a larger amount of surface area generally provides more current flow for a given voltage, reducing impedance and increasing CSC (Cogan 2008). However specific shapes may present advantages or disadvantages as well. Pore resistance may occur when there are narrow spaces in an electrode's structure that have extensive contact with the electrode, but minimal contact with the tissue. These pores reach a charge equilibrium with the electrode more rapidly than the rate at which charge passes between the pore and the tissue, reducing electrical connection between the tissue and surfaces within the pore (Posey 1966).

Penetrating electrodes are also commonly used, offering closer connections to targeted cells. This can allow for significant improvements in recording and stimulating ability as the distance between electrode and target may be greatly reduced. Applied to central nervous stimulation, penetrating electrodes can reach deeper neurons and allow for direct recording of otherwise inaccessible of the brain (Jones et al. 1992). Applied to peripheral nervous stimulation, penetrating electrodes can pass through the epineurium surrounding ganglia and axon fibers, allowing for recording and stimulation with significantly reduced noise and increased charge delivery (Micera and Navarro 2009).

Any electrodes which are implanted directly into tissue such as the brain will result in an immune tissue response which can pose a serious problem for long term use. Furthermore, this glial response may itself permanently modulate local neural signaling to reduce activity (Salatino et al. 2017; Polikov et al. 2005). This cascade continues through further stages and soon results in encapsulation of the implanted array in a "glial scar," leading to failure of chronic electrodes as they become heavily insulated from the tissue they seek to record. Because this process severely reduces electrodes' ability to both stimulate and record signals, the immune response places severe limitations on longitudinal studies (Biran et al. 2005). Smaller electrodes produce a smaller immune response (Szarowski et al. 2003), and research suggests that implants smaller than 10 µm in diameter reduce the immune response to low enough levels to offer the possibility of chronic recordings (Vitale et al. 2015).

1.3 Current Electrode Architecture

A large variety of different electrode designs are used in biomedical research and medicine. While many of the same needs and modifications are shared between different applications, fabrication methods can vary significantly. Some properties of these different architectures are listed in Table 1.

The Utah Array by Blackrock Microsystems (Figure 3) is a widely used example of a modern implantable electrode array (Maynard et al. 1997). The array is used for direct implantation into nervous tissue in the central or

Table 1: Properties of Electrode Systems

Electrode System	Material	Number of Electrodes	Geometric Surface Area per electrode	Penetrating Depth
Utah Array	Pt / IrOx	100-128	~4000 μm^2 (Straka et al. 2018)	0.5-1.5 mm
NeuroPixel Probe	Titanium Nitride	900	144 μm^2 (Jun et al. 2017)	Up to 10 mm
Deep Brain Stimulation	Platinum	4	~12 mm^2 (Butson et al. 2005)	Direct implant to Hippocampus
ECoG (AC EEG-System from IT-Med, Germany)	Stainless Steel	48-64	~12 mm^2 (Pistohl et al. 2008)	Surface
Custom ECoG (Rubehn et al. 2009)	Platinum	252	~3.1 mm^2	Surface
Carbon Nanotube Probes (Yoon et al. 2013)	Carbon Nanotube	1	~15 μm^2	0.1-1 mm
Microwire Electrodes (Mushahwar et al. 2000)	Stainless Steel	6-12	~5600-13000 μm^2	3.5-4.5 mm
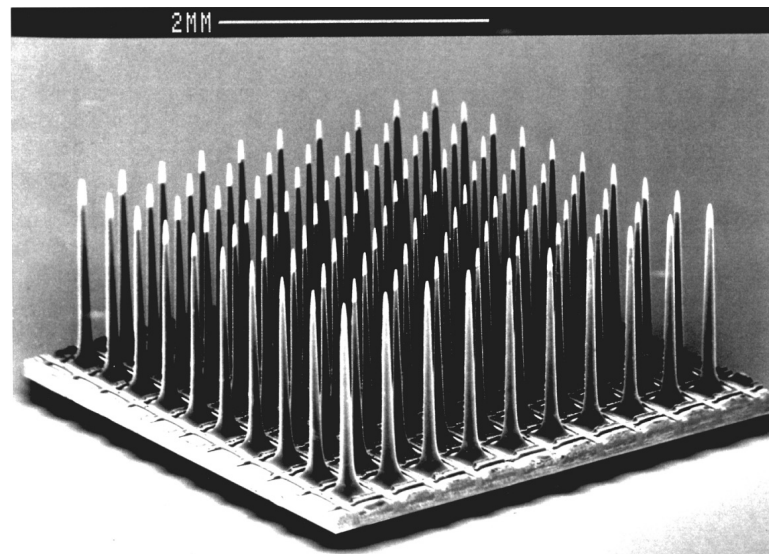
Figure 3 Utah Electrode Array showing 100 shanks with 400 µm spacing, scale bar 2 mm (Kim et al. 2006).

peripheral nervous system for long term recording in animal as well as human studies. The standard Utah Array is composed of a set of 100 electrically separate silicon shanks in a 10x10 grid, machined through use of a dicing saw and chemical etching process. The tips of the array are then coated with a conductive layer generally of platinum followed by Iridium Oxide, and then the entire array aside from the shank tips are coated in insulating Parylene-C (Blackrock Microsystems 2016). At the conductive tip, the shank diameter of the Utah Array narrows from 36 µm down towards a point, making the shanks easily large enough to cause glial scarring and severely limit chronic use. A Utah Array coated with a layer of Iridium Oxide to facilitate faradaic charge transfer shows impedance at 1 kHz in the range of 5 to 10 kOhm and charge storage capacities of 0.9 to 2.5 mC/cm2 (Negi et al. 2010). The Utah Array is fabricated through use of a dicing saw and chemical etching process, which does not allow for batch

fabrication resulting in greater variation between units and higher costs (Jones et al. 1992; Bhansali and Vasudev, 2012).

Other common silicon multi-electrode arrays such as Michigan Arrays and the NeuroPixels Probe (Figure 4) are designed to include multiple electrode contacts placed along the length of each shank to record across multiple depths (Wise et al. 1970; Jun et al. 2017). Fabrication of these arrays requires a lengthy lithography process involving 5–10 stages each requiring a µm-precision mask, a process that is very expensive and time consuming though does allow for batch fabrication (Bhandari et al. 2010). The NeuroPixels Probe is a recent development featuring 900 separate electrode contacts designed for recording, each 12 µm x 12 µm, along the length of a 10 mm shaft (Jun et al. 2017). The shank cross-section of the NeuroPixels probe are 20 µm x 70 µm, and consequently the foreign body response problem remains a barrier to their chronic use. The very large number of the NeuroPixels probe's electrodes allows for very precise localization of signals, and for simultaneous recording of a very large number of neurons. However, the very small size of these electrodes results in a higher impedance of 149 kOhm, presenting greater thermal noise problems than a larger contact might (Jun et al. 2017; Lempka et al. 2006). The NeuroPixels probe was not designed for stimulation, with the small electrode size a likely barrier to achieving high enough charge stimulation capacity for safe stimulation.

Many electrodes are fabricated as flat surfaces to be laid down directly
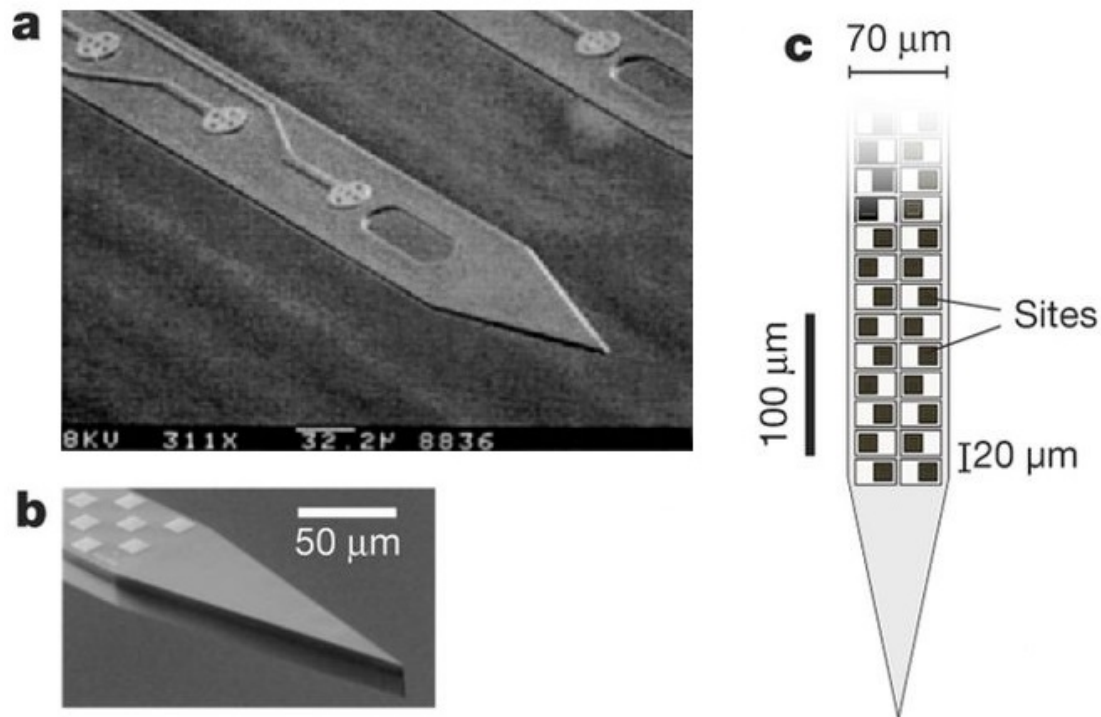
Figure 4 a) A Michigan Array shank, scale bar 32.2 µm (Kipke et al. 2003). **b)** closeup image of Neuropixels Probe shank, showing tip and recording sites, scale bar 50 µm (Jun et al. 2017). **c)** Illustration of Neuropixels Probe showing site density (Jun et al. 2017).

onto a tissue surface. Larger electrodes used for purposes such as ECG or EEG may be fabricated through a variety of methods, as the design constraints are much less restricted than for implantable devices. When a flat microelectrode is fabricated, it is generally produced as a thin film laid down through some surface deposition method such as thermal evaporation, sputtering, or chemical vapor deposition (Rubehn et al. 2009). These fabrication processes generally include multiple steps with masking and deposition stages to produce electrodes in a desired arrangement (Liu 2012). Small sets of flat microelectrodes are implanted for peripheral nerve recording and stimulation, often fabricated in flexible polymer frameworks for biocompatibility and to avoid reactions due to interactions

between stiff implants and biological tissue (Lissandrello et al. 2017).

Electrocorticography arrays (Figure 5) are sets of flat electrodes which are laid

down on the surface of the cortex below the dura, commonly used for recording

when high precision is needed in serious medical circumstances such as

identifying source regions of epilepsy. Large numbers of electrodes connected in

a flexible grid can be used to cover large areas of the brain, with electrode areas

often on the order of 1–3 mm in clinical settings (Pistohl et al. 2008; Rubehn et

al. 2009). These tools are generally limited to surface recording of larger signals

such as local field potentials as opposed to the single units that may be detected

by implantable arrays.
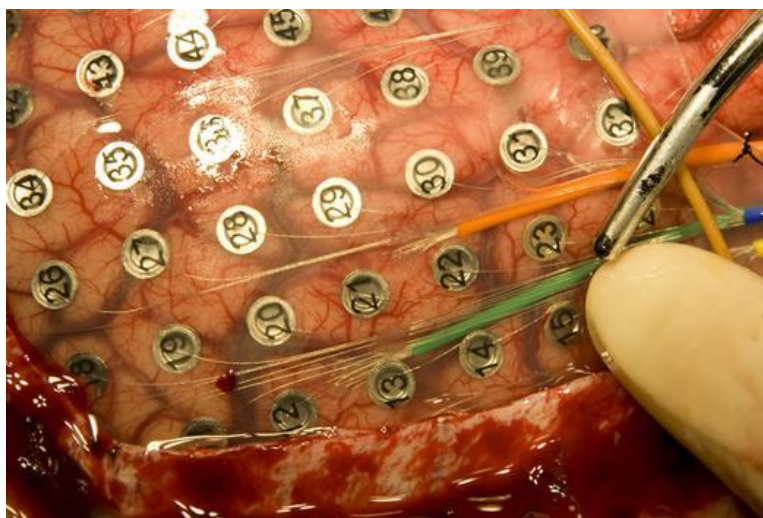
Figure 5 Implanted ECoG array (circular metal electrodes) used for epilepsy source detection (Kellis et al. 2009).

Electrodes in the form of microwires, insulated down their length except

for the tip, are also used for neural recording and stimulation (Figure 6). These

wires often have extremely small surface area, resulting in very high impedances
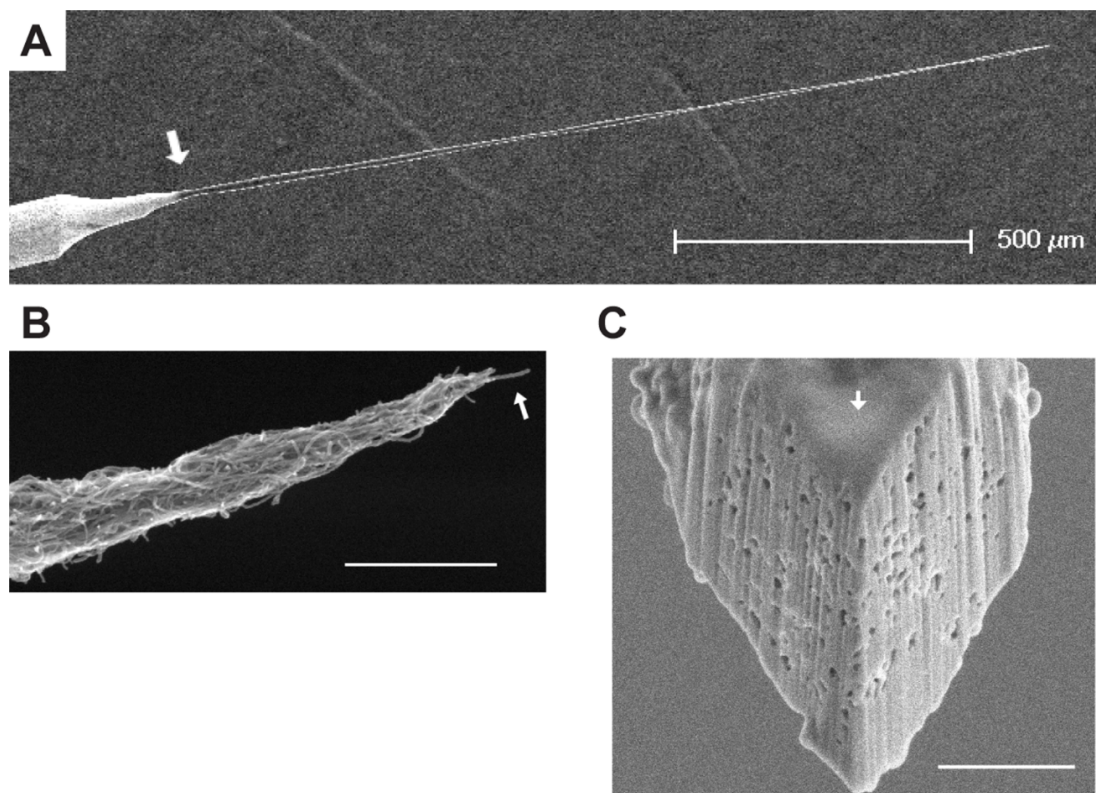
Figure 6 Carbon Nanotube (CNT) Fiber probe (Yoon et al. 2013). **a)** Low magnification view of full probe, scale bar 500 µm. Probe 1.5 mm in length. **b)** Tip of probe tapering to single carbon nanotube. scale bar 1 µm. **c)** Sharpened CNT probe tip, scale bar 1 µm.

and low charge storage. However, as they likewise can have an extremely small diameter, these wires are capable of minimizing the foreign body response of tissue. The introduction of carbon fiber and carbon nanotube fiber electrodes allows for electrode wires smaller than the 10 µm threshold needed to reduce tissue damage and immune response to levels that may allow chronic use (Yoon et al. 2013; Vitale et al. 2015). However, 5–10 µm diameter fibers made from entangled carbon nanotubes also show an impedance of over 10 MOhm, the high value due primarily to the probe's very small surface area (Yoon et al. 2013). These carbon nanotube probes were individually fabricated by drawing a

probe slowly out of a liquid solution of suspended carbon nanotubes. This fabrication process and that of other carbon fiber electrodes is very difficult and costly, preventing their regular use (Guitchounts et al. 2013). Larger microwire electrodes have been used as well, which may have a diameter closer to 30 µm or as high as 100 or 200 µm. This loses much of the benefit of reduced immune response seen at sizes below 10 µm, however it can offer lower impedances in the range of 10–30 kOhm (Mushahwar et al. 2000).

1.4 Limitations of Electrode Architecture

Because a physically smaller electrode will cause less trauma during insertion (Polikov et al. 2005) and reduction of chronic foreign body response (Gällentoft et al. 2015; Salatino et al. 2017), there has long been a push for miniaturization. Further motivating this trend, smaller electrode geometries can allow for more densely packed arrays with a larger number of distinct active sites and provide higher specificity in targeting an area for stimulation through their smaller points of contact (Sekirnjak et al. 2008). However because miniaturization decreases the available surface area through which current and therefore charge can flow, impedance increases and the voltage necessary to achieve the same amount of stimulation increases as well. As a result, this miniaturization presents barriers to overcoming thermal noise in recording and to achieving sufficient charge injection for stimulation without inducing tissue and electrode damage (Cogan 2008).

Another significant barrier to miniaturization is fabrication requirements.

The fabrication of extremely small devices presents new challenges, with micrometer electrical designs often requiring high quality clean rooms which present extremely high manufacturing and packaging costs (Liu 2012). Other methods which have less extreme infrastructure requirements such as the dicing saw approach used in the Utah Array fabrication process present reproducibility challenges and make batch fabrication difficult, retaining high costs in other areas (Bhandari et al. 2010).

While most electrodes are fabricated as either flat surfaces or straight shanks, this is to some extent a result of challenges in fabrication rather than for minimization of impedance (Jones et al. 1992). Classic thin film lithography processes used for Microelectromechanical Systems (MEMS) devices which are in common practice for batch fabrication of flat electrodes are only capable of producing slopes or rounded forms under certain specific conditions of direction and material, and require very large numbers of steps to perform, increasing cost and fabrication time (Liu 2012). As this space has been constrained by these fabrication limits, there may be suitable electrode shapes that offer a higher RSA and consequently improved impedance and CSC when compared to a flat or pointed electrode of equivalent GSA, but which are not manufactured due to difficulty and cost.

1.5 Surface Modification Techniques

To address the limitations of electrode architecture, techniques have been developed which can be applied after fabrication to attempt to improve recording

quality, overcome disadvantages of miniaturization, or directly address other challenges to electrode use.

One set of such techniques is directed towards improving impedance and CSC by the addition of a final modification step. One most widely used technique is to add a thin layer of faradaic charge-injection material onto an electrode to improve charge transfer. Materials such as Iridium Oxide and Platinum Iridium alloys are capable of efficient faradaic charge transfer, and will commonly be added as a final coating to an electrode fabricated with a primarily capacitive base material such as gold (Cogan 2008; Deku et al. 2018; Weiland et al. 2002). IrOx and PtIr layers are often deposited as a final coating, as are conductive polymers such as PEDOT:PSS. This is especially effective at improving CSC, though the introduction of faradaic charge transfer does introduce the risk of irreversible redox events if large charges are delivered too rapidly which can degrade electrodes as soluble compounds are produced. Adding a coating stage to electrode fabrication introduces its own challenges as well, as coating stability may be less robust than the underlying electrode, introducing new risks of the surface cracking and flaking over time (Cogan et al. 2004; Negi et al. 2010). As these layers are general tens or hundreds of nanometers thick, they do not contribute significantly to electrode size. These methods are capable of improving CSC of electrodes as much as 1.5x to 10x original values, depending on the base electrode material and coating parameters such as thickness and deposition method (Deku et al. 2018; Cogan

2008; Pranti et al. 2017; Robblee 1983)

Surface roughening methods are sometimes used to increase the RSA of a conductive surface without affecting its GSA, reducing impedance and increasing charge storage capacity. These high roughness surfaces may be produced directly due to the nature of a fabrication method, as in the case of high roughness Titanium Nitride sputtered electrodes (Weiland et al. 2002), or through a standalone process, such as electrochemical surface roughening (Arroyo-Currás et al. 2017). Though at times these surface area increases are difficult to quantify precisely, Arroyo-Currás et al. report as high as a 2-fold increase in RSA with their electrochemical roughening technique, and show a subsequent improvement in charge storage capacity. However, these roughening techniques present their own limitations. When applied to thin film electrodes, roughening runs the risk of exposing underlying surfaces of the substrate which will not have the desired conductivity, and may present other biocompatibility problems or electrode longevity problems. Additionally, as increases in roughness create steeper and narrower surfaces, pore resistance begins to result in diminishing improvements as the sections of the electrode that are located within narrow deep openings no longer effectively contact the tissue (Arroyo-Currás et al. 2017; Posey et al. 1966).

While a twofold increase is significant, the charge injection needs presented by extremely small electrodes require a greater than twofold improvement, making this not a complete solution to the miniaturization

challenge. Changes in the larger electrode design present a possible area for further investigation: Simulation of three-dimensional electrodes and penetrating electrodes have shown that the reduction in distance to the targeted cell can result in a reduction in impedance (Joye et al. 2009; Heuschkel 2001). The fabrication of electrodes as three-dimensional structures optimized for surface area on the micron resolution scale could provide an entirely new scale in which to make RSA-increasing designs, smaller than electrode dimensions but larger than surface roughening. This approach would also be possible to perform in parallel with methods such as surface roughening and IrOx coating, to result in further improved impedance and CSC and therefore potential for smaller, readily fabricated microelectrodes.

2 Materials and Methods

2.1 Objectives

The goal of this work was to develop a method to improve the impedance and charge storage capacity of a given electrode without changing its footprint. Impedance and CSC were measured through electrochemical impedance spectroscopy (EIS) and cyclic voltammetry (CV) respectively. As a prerequisite to any observable improvements, a process flow had to be developed and each of its steps tested for reliability and efficacy. This led to additional requirements such as all or most prints surviving every step of the fabrication process from printing to final characterization, and laser etching capable of reliably removing gold thin films.

Once the fabrication process could be demonstrated as successful, any consistent pattern of improvement observed for electrode pads from before to after the fabrication process could be considered a sign of success, measured as a statistically significant reduction of impedance and/or increase in CSC. Further tests could then be pursued including tests of attachment strength, durability, biocompatibility and others.

As an additional aim, the experiments performed pushed boundaries of established uses for Two Photon Direct Laser Writing (DLW) printing. The DLW printer used presented different parameters from other DLW printers in common use, the full significance of which had not been fully explored. As it became apparent that the rDLW system had a capability to print on reflective opaque

surfaces such as gold, something unfeasible with other DLW systems (Rekštytė et al. 2014; Žukauskas et al. 2013), investigation into this phenomenon became an additional priority.

2.2 Tools and Techniques Used

2.2.1 Process Flow

To achieve an increase in RSA without significantly changing the GSA of an electrode, a process was designed to increase electrode surface area by vertically extending a thin-film flat electrode into a three-dimensional structure (Figure 7). This was accomplished through a series of steps beginning with the use of a resonant scanning direct laser writing (rDLW) printer to fabricate acrylic polymer structures with high surface area or other desired geometries on the surface of a target electrode pad. Once a high surface area structure was fabricated on the electrode surface, the structure was then metallized through a gold sputter deposition process, producing a conductive film across the full surface of the printed structure. Lastly, a laser etching step using the same rDLW system without polymerizable medium was performed to remove unwanted sections of the gold thin film that were deposited in areas other than the desired electrodes during the unmasked sputter deposition process. Electrodes were characterized through electrochemical impedance spectroscopy and cyclic voltammetry before and after this process was carried out, so that changes in individual electrodes could be evaluated. Some electrodes were left without

Process Flow

1. Initial electrode

2. DLW Printing

3. Sputter Deposition

4. Laser Etching

Figure 7 Illustration of four step process flow for electrode modification.

prints but underwent the same sputtering and etching process to serve as a control.

The electrodes used were fabricated on 100 mm Si (1 0 0) wafers, with deposited layers of polyimide (1 μm) and silicon carbide (2 μm). The conductive layer of the electrodes was produced by sputtering deposition of titanium (30 nm), gold (250 nm), followed by a second layer of titanium (30 nm), followed by another insulating 2 μm layer of silicon carbide. The top layers of silicon carbide and titanium were then etched using SF6 plasma to expose the gold electrode surface (Deku et al. 2018).

2.2.2 Resonant Direct Laser Writing

Fabrication of micron scale polymer structures with Direct Laser Writing

lithography is well established field (Maruo et al. 1997; Kawata 2001; Cumpston

et al. 1999; Selimis et al. 2015). As these systems use computer aided design

models, there are very few limitations on possible shapes which can be printed

allowing for the rapid creation of complex geometries in a variety of

polymerizable substrates (Atwater et al. 2011; Bückmann et al. 2012; Farsari and

Chichkov 2009; Niesler and Tanguy 2015; Sun and Kawata 2004; Skylar-Scott et

al. 2017). The resolution of this method is sufficient to allow for the fabrication of

optical lenses from transparent polymers, with print surface roughnesses of 30

nm or below if using tailored equipment (Gissibl et al. 2016; Belazaras et al.

2010).

DLW printing technology is based on two photon polymerization (2PP),

where a tightly focused laser is pulsed at femtosecond speeds while being

scanned through a polymerizable liquid. The wavelength of the laser is selected

to be twice the polymerization wavelength of the photopolymer, such that only at

the laser's focal point is the concentration of laser light high enough for

simultaneous activation by multiple photons and therefore polymerization to

occur. As the laser is swept through the photopolymer through use of a

galvanometric mirror often accompanied by the movement of a piezo-stage,

these pulses produce voxels which can achieve features as small as 150 nm or

lower in each dimension. Restrictions in print geometry are minimal, with

overhangs or unattached objects presenting challenges of temporarily lacking attachment during printing, but these challenges can be easily addressed through classic 3D printing methods of introduction supports as needed.

For this project, a raster-scanning direct laser writing printer was used (Figure 8) (Pearre et al. 2018). This system uses a resonant mirror scanning at 8 kHz, bringing the printer's speed up to 8000 mm/s, tens to thousands of times faster than other high-speed galvanometer based DLW printers (Obata et al. 2013; Maruo and Ikuta 2000; Gottman et al. 2009; Farsari et al. 2006; Žukauskas 2013).

Visualization was achieved through light provided by a tunable Ti-Sapphire laser. The lens was submerged in the dip-in polymerizable photoresist used for printing, IP-Dip (Nanoscribe GmbH, Germany), which is highly
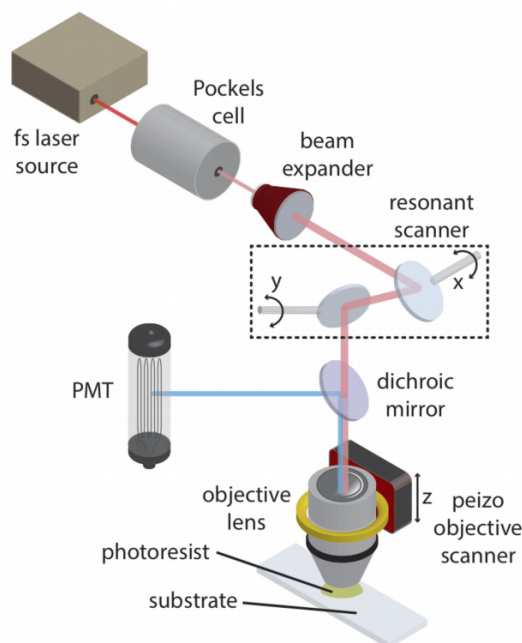
Figure 8 Optical path schematic for rDLW printer (Pearre et al. 2018).

fluorescent when observed at laser power below the IP-Dip polymerization threshold allowing for visualization of the target surface and precise alignment of the prints. Polymerization of the liquid IP-Dip photoresist for structure printing was performed using the same laser system (~120 fs pulse duration, 80 MHz repetition). While the use of other photoresists was possible, IP-Dip was selected as it matched the index of refraction of the lens used as well as having a polymerization wavelength of 390 nm, half the wavelength of the laser used, allowing for two photon polymerization. Pump laser power was held at 9 W, using a mode-locked output beam at 780 nm. A Pockels cell and 3.33-MHz DAC were used for modulating beam intensity throughout the raster scan.

The extreme resolution and open-ended scope of possible print geometries offered by DLW gives it some advantages over existing microfabrication methods. MEMS process flows make use of many-step sequences of layering, masking, and etching to produce structures of similar resolution, however this process is extremely time consuming and expensive, requiring a large array of high-end equipment, clean room conditions, and complexly designed process flows that are limited to certain combinations of geometries and materials. It is usually impractical, for example, to fabricate curved surfaces using standard MEMS techniques as fabrication occurs in discrete layers, each of which may require several steps of process to shape through masking and etching processes (Liu 2012). MEMS process flows do offer several advantages over DLW printing alone, first and foremost the

fabrication of a wide array of materials, including metals. However, the combination of DLW printing with MEMS metallization techniques such as sputter deposition or chemical vapor deposition may allow for the controlled fabrication of new structures with fewer steps and lower costs than by any existing methods.

One major limitation of traditional DLW printing is its inability to successfully perform prints on opaque reflective surfaces, including metals (Rekštytė et al. 2014; Žukauskas et al. 2013). Most printing is performed on transparent substrates such as glass as direct printing onto opaque reflective surfaces leads to a destructive phenomenon which is theorized to be a result of dielectric breakdown caused by an increase in laser ionization due to the reflection off the surface (Malinauskas et al. 2010). This breakdown will at best result in significant distortions of the desired shape, and at worst will cause highly disruptive 'micro explosions' due to reflection of the laser light from the substrate increasing power and heating across an area which can destroy large portions of the intended structure (Figure 9) (Rill 2008; Tanaka et al. 2006; Rekštytė et al. 2014; Žukauskas et al. 2013). In most cases, severe dielectric breakdown results in structures that are incapable of bonding to the substrate due to their degree of fragmentation, and cannot be imaged as they are washed off during development.
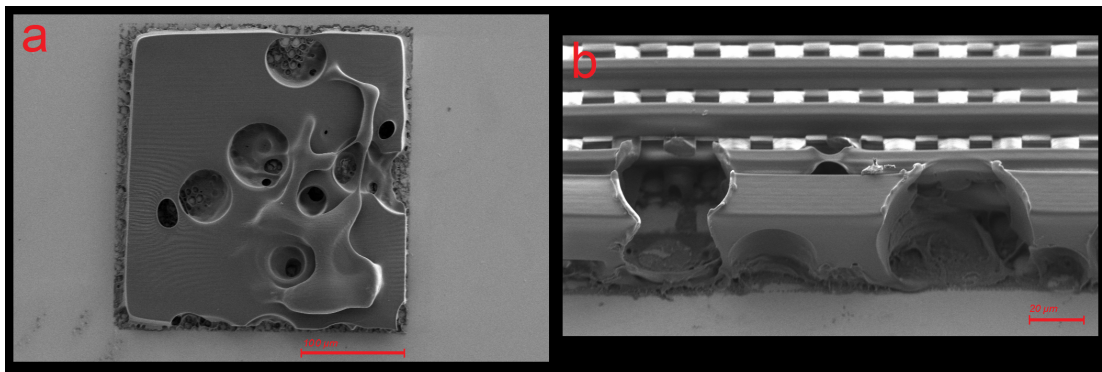
Figure 9 SEM images of structures displaying limited dielectric breakdown. These structures suffered only very minor damage from the micro explosion effect, resulting in structures that survived development but with significant distortion. These structures were printed with the rDLW system at depths intentionally placed partially below the substrate surface by 10 μm or more, causing focusing to occur into the reflective surface and ensuring excessive reflection and subsequent dielectric breakdown. Both structures were printed on / below a substrate of 150 nm gold thin film sputtered on silicon. **a)** Scale bar 100 μm. **b)** Scale bar 20 μm.

This limitation has been overcome through use of the rDLW printer, which is believed to be a result of its significantly increased scanning speed. An increase in scanning speed results in a proportionally reduced amount of time for polymerization to occur. However as two photon polymerization events depend on the square of excitation intensity (Benninger et al. 2013) a 100-fold increase in scanning speed only requires a 10-fold increase in laser power to produce the same polymerization. As a result, the total amount of energy being delivered to the polymer liquid during each pass of the laser is significantly reduced in the rDLW system.

Another proposed explanation for the reduced breakdown observed is that laser etching of the gold substrate is occurring during the print process, preventing breakdown by removing the reflective source at the point of printing. While this has not been directly tested at this time, this is inconsistent with later

a

b
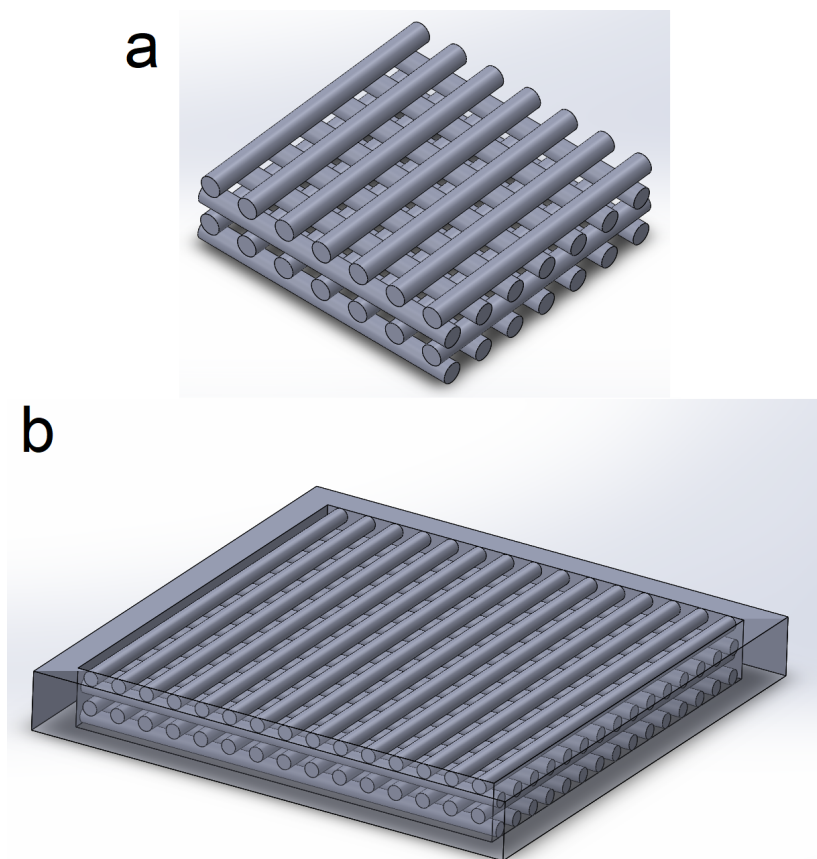
Figure 10 Design files of log pile structures with and without walls used to demonstrate print quality. Spacing between bars is equal to bar diameter, with this value customizable during the print process.

observations of the printer's inability to effectively etch gold thin films of higher

thicknesses while printing on these surfaces remains possible.

This new capability for printing on reflective substrates opens the door to

the electrode fabrication and modification techniques described in this thesis, as

well as a wide range of other potential applications.

2.2.3 Print Designs

Using DLW printing, the introduction of new print geometries is matter only

of producing an STL file with the desired structure through use of any common

CAD software. In this case, Solidworks was used for the structures designed. A wide variety of structures were designed and used during this thesis, as suited to different goals.

The first class of structures used in this thesis were designed for purposes of demonstrating the rDLW printer's capability of printing on opaque reflective surfaces. These were modeled based on previous demonstrations in literature which showed the challenges of achieving this same goal, and included logpile cross hatched structures (Figure 10), and simple cubes with known gaps.

A second class of structures was designed to demonstrate the printer's ability to replicate penetrating electrode forms. As penetrating electrodes can allow for significant improvements in recording and stimulating ability over surface electrodes, this was considered to be a particularly beneficial structure to fabricate. Simple conical spikes were modeled for printing at a range of angles and base widths.

A third class of structures was designed to be printed on an existing flat electrode surface with the goal of increasing real surface area (Figure 11). These structures would be printed on the surface of existing electrodes, then coated using sputter deposition to produce a conductive surface area larger than that of the original electrode. As sputter deposition is a moderately directional deposition method, structures were designed to avoid any overhangs or hollows that would not have a direct line of sight between the surface of the print and the deposition source during sputtering. Given this limitation, increases in surface
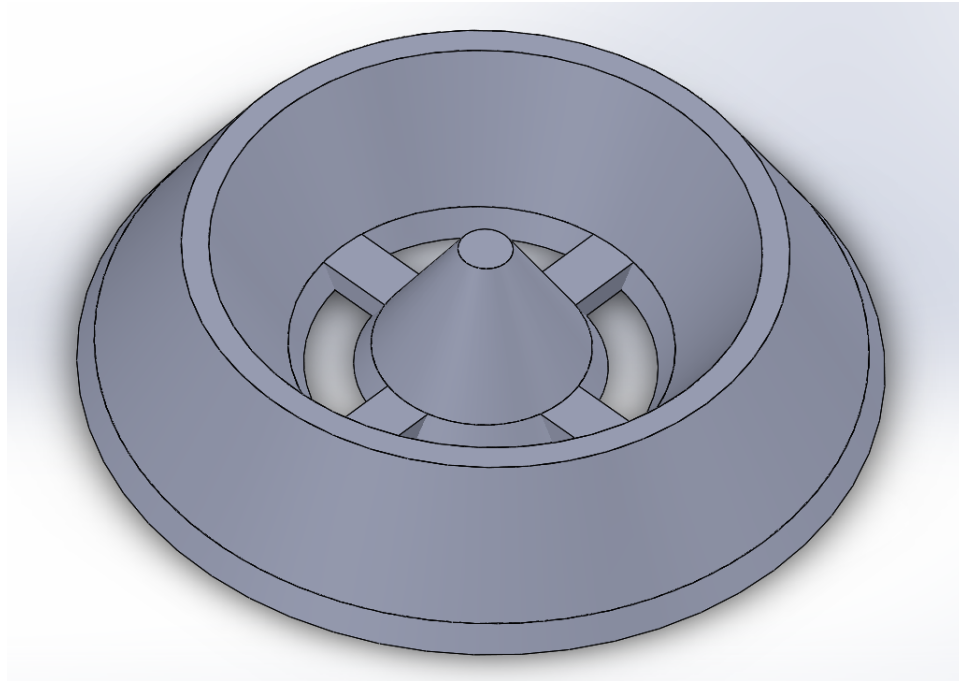
Figure 11 Structure for electrode improvement. 79% of the footprint of this structure is sloped. When fabricated with a height equal to 50% the structure's diameter this produces angles of 76.5 degrees and a surface area increase to 340% that of a flat electrode with the same GSA.

area were accomplished through the design of 3D structures featuring extensive

sloped areas. By printing sloped surfaces over large portions of the electrode's

footprint at steep angles, it was possible to significantly increase the real surface

area contained within the outline of the electrode. The high resolution of the

printing process allowed for sloped surfaces of more complex geometries than a

simple cone, achieving high surface areas without large height differences

between the highest and lowest points. Prints included small horizontal areas to

optimize sputter deposition as well as openings in the print to allow additional

areas of electrical contact between the surface coating and the electrode pad.

During this thesis these structures were fabricated with heights of 40%, 50% or

60% of the diameter of the electrode pad, with the structures having an resulting

surface area of 278%, 340% or 406% of the original flat surface area respectively.

While RSA increases have been shown to reduce impedance and increase CSC (Arroyo-Currás et al. 2017; Harris et al. 2018), the effect of electrode shape on impedance and charge storage capacity presents a complex modeling problem that must account for differing voltage distribution across the surface of an electrode (Joye et al. 2009). As a result, quantitative predictions for improvement amounts were limited to estimating an improvement proportional to surface area, as seen in flat electrodes of varying sizes (Harris et al. 2018).

2.2.4 Metallization

To render the IP-Dip polymer structures printed usable as electrodes they must be electrically conductive. Common electrode metals which could be used for this process include gold, titanium nitride, platinum, and stainless steel. Gold was selected as the preferred coating material because it is a common biomedical electrode material and to ensure a fair comparison between pre and post process characterization, as the wafer-based electrodes tested feature gold electrode pads.

Sputter deposition was selected as a metallization method for its ease of use: it is an inexpensive, rapid, highly controllable method of thin film generation which can be easily used with a gold target. Sputter deposition is a widely used method of film layering across large surfaces. A species of physical vapor deposition (PVD), in which inert gas particles such as argon are made positive
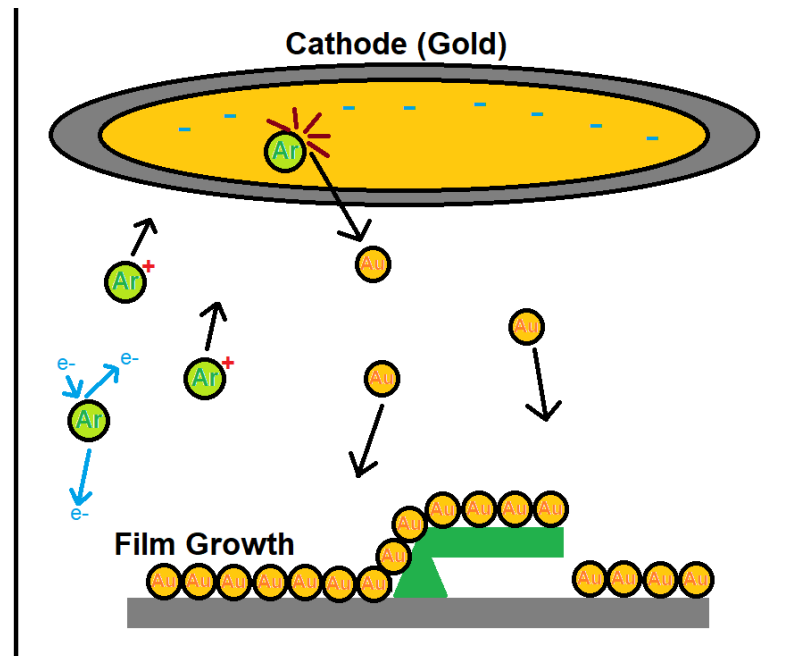
Figure 12 Diagram of the sputter deposition process, in which argon is accelerated to strike the sputtering target cathode at high speed, ejecting gold towards the sample to be coated. Covered areas beneath overhangs or other structures will be shadowed, preventing coating.

through electron collisions then accelerated by electric field to extremely high speeds whereupon they impact a target of the desired thin film material, in this case gold. Atoms are ejected from the target at similarly high speed and travel in a straight line to impact and remain on all exposed surfaces (Figure 12). Sputtering as a technique is commonly used with gold and gold-palladium alloys for coating objects to be imaged in a Scanning Electron Microscope, and can be used more broadly to deposit films of many different materials, including pure metals as well as nitrides or oxides (Liu 2012).

Once gold thin films reach a thickness in the tens of nanometers, possible within minutes in a sputter coater, they reach a resistivity on the order of 10^{-3} Ω/m, sufficiently conductive to carry the currents on the order of 100 µA and

below in use with these electrodes (Zychowicz, Krupka, and Mazierska 2006).

However, as it is hard to mask for sputter deposition at such small sizes, efforts

must be made to prevent or remove unintended electrical connections between

adjacent electrodes (Kummamuru et al. 2008).

Sputtering was performed using the Cressington 108 Sputter Coater using

a gold target. Estimates of film thickness were based on the working

specifications of the device, with a 3 mm distance from the target and 20 mA

current producing a sputtering rate of 0.5 nm / s. Substrates for demonstrations

of printing on gold were produced, with a 40 nm film on glass and a 150 nm film

on silicon. Sputtering on printed structures on electrodes was performed at 30-

40 nm.

2.2.5 Laser Etching of Sputtered Films

The introduction of a thin film over a large area of the sample, including

two dozen adjacent electrode pads at a time, necessitated the development of a

reliable and precise method of electrically separating these sites after sputtering

was complete. Laser etching is a well-established method for the removal of

gold thin films without damaging the underlying substrate (Miller et al. 2004,

Rohde et al. 2013). This etching process was accomplished using the same

rDLW printer equipment that was used for polymerization of structures, using a

5% by weight Dextran-Fluorescein saline solution as the dip-in medium instead

of IP-Dip photoresist. This fluorescent medium allowed for the visualization of

the wafer surface without polymerization. Prints were then located and etching

was performed by activation of the laser in the same manner used for polymerization of structures, following a pattern designed to etch an area around the perimeter of each electrode pad. Etch prints were passed over the targeted areas five times to ensure a complete removal of the conductive film. This electrically separated each pad from the rest of the sputtered thin film on the wafer without damaging the conductive coating on the prints and pads themselves.

2.2.6 Characterization

Electrodes were characterized before and after the printing process. All characterizations were performed using a Gamry Instruments Reference 600 potentiostat using vendor supplied software. Electrodes were submerged in pH 7.24 Phosphate Buffered Saline (PBS) solution, with a large platinum mesh counterelectrode and Ag/AgCl wire reference electrode. After being submerged, electrodes were left for ~15 minutes to reach equilibrium.

Each pad in turn had one electrochemical impedance spectroscopy test, then one cyclic voltammetry test. Once all pads in a set of 12 were tested once, this was repeated. Once all pads in the set of 12 had been tested twice, a third set of EIS tests was run. This process was performed one time before the full printing, sputtering, and etching process flow and one time afterwards. We report this order of measurements to ensure standardization of amount of time electrodes were submerged.

Electrical impedance spectroscopy was conducted at each decade

between the frequencies of 10^2 Hz and 10^5 Hz at an AC voltage of 0.1 mV rms.

Cyclic voltammetry was performed between water window limits of -0.6 and 0.8 V, with a scan rate of 50 mV and step size of 10 mV. Three cycles were recorded each time the CV procedure was run with cathodal CSC calculated by averaging the negative current integral of all runs other than the first. The first run was thrown out before averaging as the first pass of a CV process contains increased amounts of error as equilibrium is reached, being visibly distorted when compared to all subsequent runs.

3 Results and Discussion

3.1 Printing on Opaque Reflective Surfaces

Figure 13 shows SEM images of prints taken on gold film substrates with different thicknesses and base materials. Reliable fabrication of logpile structures with bars of widths ranging from 3 to 10 μm is demonstrated, as well as sharp edges in rectangular shapes. While slight curved distortions occurred at the far corners of the largest prints due to the distortions of the printer's optics at the edges of its print area, lines at the center of the prints show high quality without distortion, including gaps as small as 4 μm wide between solid structures of 40 μm height as shown in figure 13b.

Figure 13b also shows small residual connections between the printed cubes. As areas near the focal point still receive some illumination through both limits of focus and scattering, it is possible that these connections are small unintended polymerization events that formed during printing within the gap between the intentionally polymerized structures.

Intact, high-quality prints were reliably possible when initial print depth was placed near but not below the surface of the substrate. Prints placed deep below the reflective surface at depths of 50 μm often showed extensive dielectric breakdown and micro explosions in a similar manner as other DLW systems (Figure 14). However, prints placed at a depth of only ~5 μm below the surface showed highly reduced breakdown, with only minor distortions. The increase in breakdown with depth is believed to be a result of the repeated scanning over the
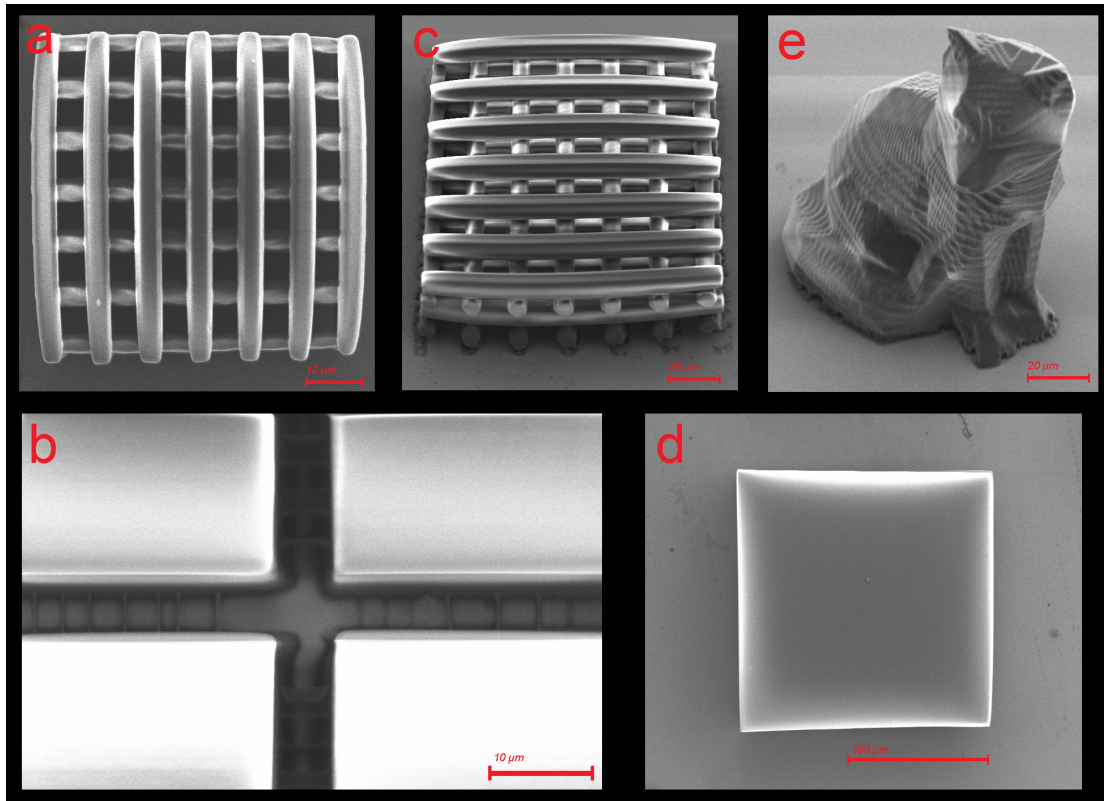
Figure 13 SEM images of structures printed on gold surfaces using rDLW printing with IP-Dip polymer. **a)** Log pile structure printed on 40 nm gold thin film sputtered on glass, scale bar 10 μm. **b)** Boxes with 40 μm height and precise spacing printed on 40 nm gold thin film sputtered on glass, scale bar 10 μm. **c)** Log pile structure printed on 150 nm gold thin film sputtered on silicon, imaged at 33 degree angle, scale bar 20 μm. **d)** Square box printed on 150 nm gold thin film sputtered on silicon, scale bar 100 μm. **e)** Fox model printed on 150 nm gold thin film sputtered on silicon, scale bar 20 μm.

reflective surface in the deeper cases. With a height resolution of 1 μm, a print

that begins 50 μm below the substrate surface will scan the laser over the

reflective substrate 50 times before the focal point reaches the polymer.

This demonstrates that DLW printing on reflective metal substrates is

achievable. This is in contrast to previous literature which demonstrated only

limited printing under controlled conditions, with specially prepared low-reflectivity

substrates (Žukauskas et al. 2013). The rDLW system used for printing is similar
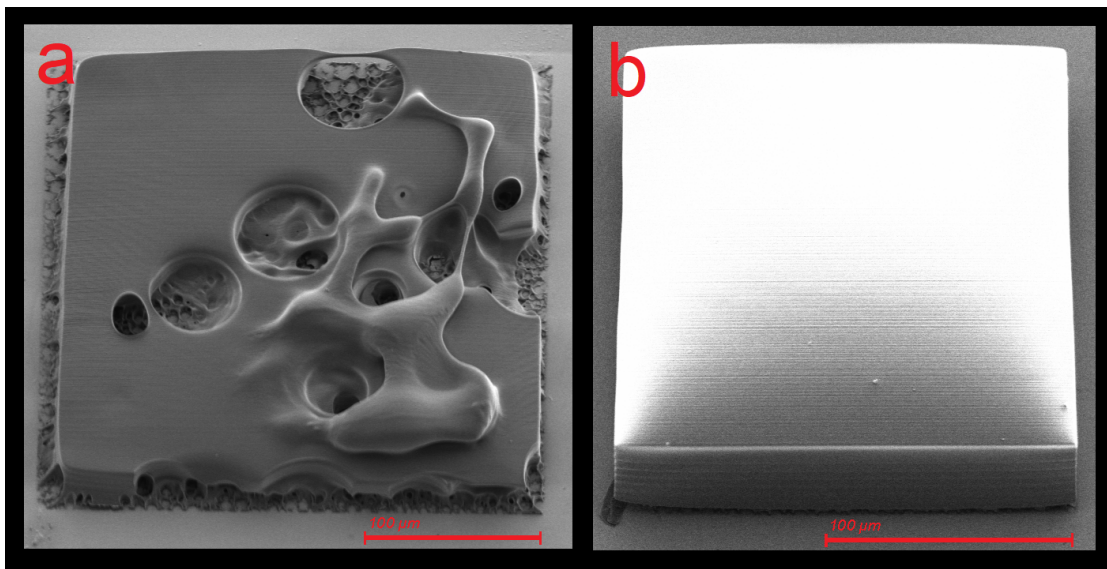
Figure 14 SEM images of square box structures printed on 150 nm thin film of gold sputtered on silicon. The structure in **a)** A featureless box printed at a depth of 50 μm below the substrate, showing distortions due to dielectric breakdown effect. Scale bar 100 μm. **b)** A featureless box printed near and slightly above the surface of the substrate, showing no dielectric breakdown. Scale bar 100 μm.

to commercially available DLW systems which are widely used elsewhere. The most prominent difference is the scanning speed with the rDLW system as much as three orders of magnitude faster than what is in common use. As this high scanning speed results in the laser spending less consecutive time focused on any given location during the print process we theorize that this reduced exposure prevents concentrations of laser energy that lead to dielectric breakdown events, resulting in the ability to produce prints without damage as shown above. Unfortunately, the design of the rDLW system used prevents large adjustments in speed as the resonant mirror used is not adjustable, so it was not possible to validate this theory by printing at 1000x lower speeds as in other literature while keeping other parameters of the rDLW system the same. This

would be a valuable experiment to perform in the future, but will likely require the creation of a new speed-adjustable rDLW printing system.

These prints demonstrated a high attachment strength to the substrate. When printed at the appropriate height near the surface prints demonstrate a very high rate of retention, persisting through two rinse stages of development and extensive handling through examination under optical microscope and SEM, as well as repeated submersion in electrolyte for characterization. During the process of this research using the circular surface area prints shown above, no print was observed to detach from an electrode pad after development at any point during the work. Exact attachment strength has not been quantified on gold at this time due to the difficulty of acquiring a force meter that can act on the sizes of objects involved with control over direction of applied force. However, two preliminary tests showed that an IP-Dip print on glass with a 300 μm x 200 μm footprint was capable of supporting 1.28 g of hanging weight without separating from the substrate.

This capability opens up new possibilities in fabrication. There are many devices which are not practical to fabricate without the ability to perform printing on reflective and opaque surfaces. The single-step ability of the DLW print process fabricating complex polymer structures on conductive surfaces has the potential to produce enormously more efficient process flows for microsystem fabrication. Many MEMS microactuators and microsensors use electrical forces or conductivity to perform their intended actions, and require complex

arrangements of polymers and conductive surfaces to achieve these ends, often requiring process flows requiring a dozen or more steps (Liu 2012).

Wire bonding is a major process in integrated circuit and semiconductor manufacturing, and presents challenges at the micron scale. The described method could be used for printing connections between electrical surfaces which could then be metallized, or for the printing of metal-doped conductive polymers directly for use as wires.

Metamaterial research has made extensive use of DLW fabrication for its methods, and also regularly involves layers of metallic or semiconductor coatings. The ability to print directly on metal may make these fabrication processes simpler or even introduce new designs that could not be produced otherwise.

The high resolution and customizable design of DLW printing makes it well suited to the fabrication of microfluidics systems. Such systems often make use of metal-based sensors including electrochemical sensors such as those described above. The ability to directly incorporate these sensors by printing microfluidic structures around them in a single step could provide an efficient fabrication method for these systems.

In addition to modification of electrodes, these techniques could be applied to electrochemical aptamer based (E-AB) biosensors to improve their surface area and thereby their efficacy. Any other application requiring an increase of surface area for microstructures could benefit similarly.
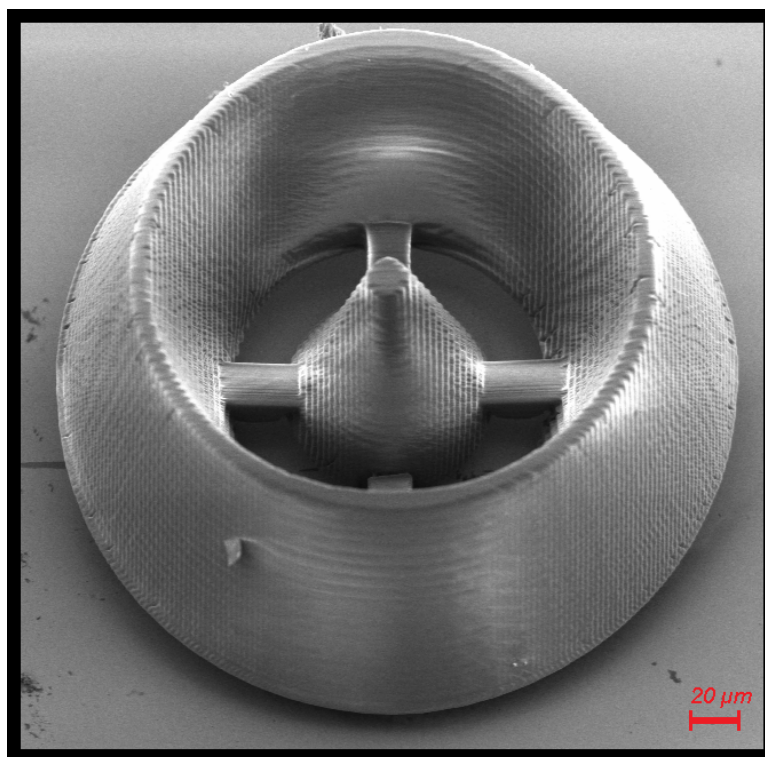
Figure 15 SEM image of the structure design used for increase of surface area. Openings in interior were left to create additional possible points of connection with substrate. Scale bar 20 µm.

3.2 Modified Electrode Characterization

Electrodes were characterized in sets of 12. While many batches of electrodes were very consistent, some batches showed high variability between measurements on the same electrode or between electrodes of the same size, and are not reported as we believe they represent electrode sets with fabrication flaws or damage from handling. Percent change in properties for each electrode was determined by comparing the mean value from before-print measurements (three impedance and two CSC for each electrode) to the mean value of after-print measurements, sputtering, and etching. Electrode pads that were used
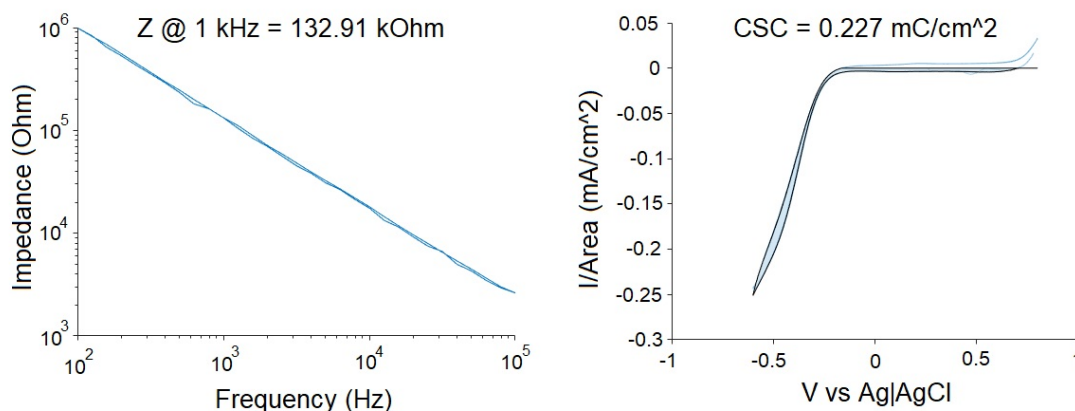
Figure 16 Plots of impedance and charge storage capacity from a 100 μm electrode before modification. **a)** Electrical impedance spectroscopy graph showing the expected linear relationship and an impedance value consistent with other 100 μm diameter gold electrodes. **b)** A cyclic voltammetry measurement showing the expected long tail, with a charge storage capacity within the expected range and consistent with other measured pads.

were 34 μm, 50 μm, or 100 μm in diameter. Figure 15 shows an SEM image of a printed structure of the kind used for surface area increase on electrodes.

Electrical impedance spectroscopy measurements were expected to form a consistent linear slope in log-log plotting of frequency vs. impedance magnitude between frequencies of 10^2 and 10^5 Hz. This result was observed in almost all cases, with only 1 of 36 electrode pads used consistently showing distorted results before and after printing, with similarly divergent impedance values (Figure 16a).

Cyclic voltammetry measurements of charge storage capacity produce a curve which is generally smooth during successful measurement, with gold contacts known to commonly produce a plot featuring a long narrow tail (Figure 16b) (Burke et al. 1997). While most values fell within a range from 0.1 to 0.6 mC/cm^2 a small number of electrodes consistently produced results significantly

Figure 17 a) Mean impedance values from each 100 μm electrode pad on one wafer, before printing, sputtering, and etching process. Three measurements were taken and averaged from each pad to produce each point shown. Some pads were not printed on but still underwent the sputtering and etching process to serve as comparisons. **b)** Mean charge storage capacity measurements from the same set of 100 μm electrode pads.   Two measurements were taken and averaged from each pad to produce each point shown.

removed from this range, below 0.01 or above 2, always combined with distorted

CV curves, and were not used.

The average measured values for the 100 μm pads from one wafer are

shown, before and after printing, in Figure 17.

35 electrode pads had their Impedance values compared before and after

the printing process, 12 without a structure printed and 23 with a structure

printed. 26 electrode pads had their CSC values compared before and after the

printing process, 8 without a structure printed and 18 with a structure printed

(Figure 18). Pads which went through the sputtering and etching process but did

not have a printed structure showed a mean lowering of impedance of 38.6% (p
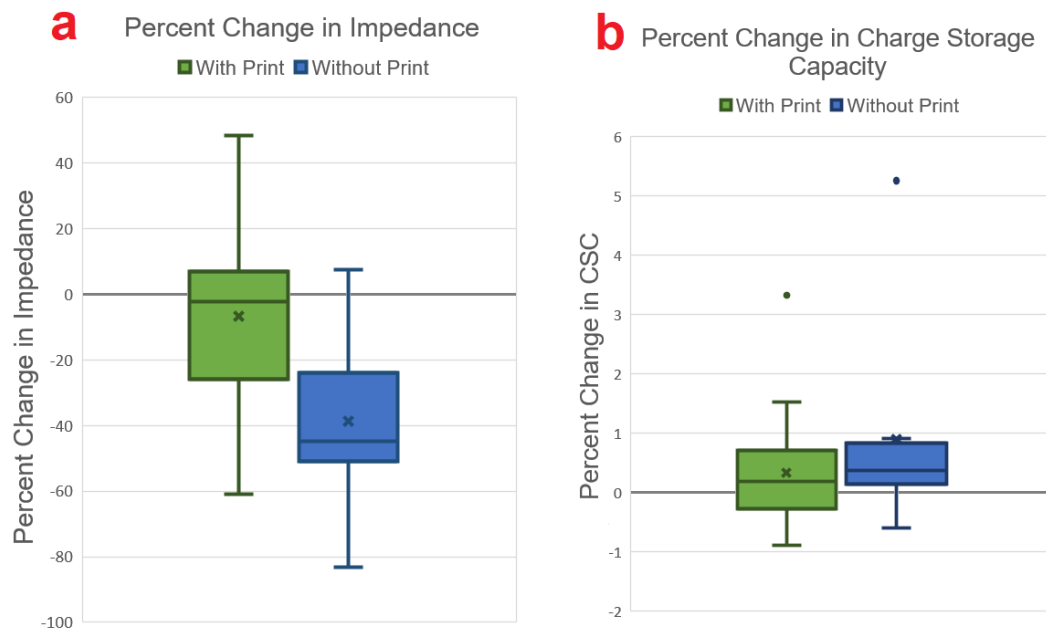
Figure 18 a) Quartiles of percentage change in impedance. The With Print plot (n = 23) shows the percentage change in impedance for electrode pads which had structures printed, sputtered, and were then etched to remove electrical shorts. The Without Print plot (n = 12) shows the percentage change in impedance for electrode pads which were only sputtered and then etched to remove electrical shorts. The central lines in each plot indicate the median value, and the x indicates the mean value. **b)** Quartiles of percentage change in charge storage capacity, as in a. With Print plot (n = 18), Without Print plot (n = 8).

< 0.001) from before the process to after, compared to no statistically significant change for pads that did have a printed structure. A two sample two tailed t-test additionally shows a significant difference (p-value < 0.001) between changes in impedance for pads with a print and changes in impedance for pads without a print. We did not find that the electrode pads with a print showed a greater reduction in impedance. Rather we observed that impedance decreased further in pads with no print. Charge storage capacities showed a wider variation in both direction and magnitude of change, with no statistically significant difference between pads with and without printed structures.
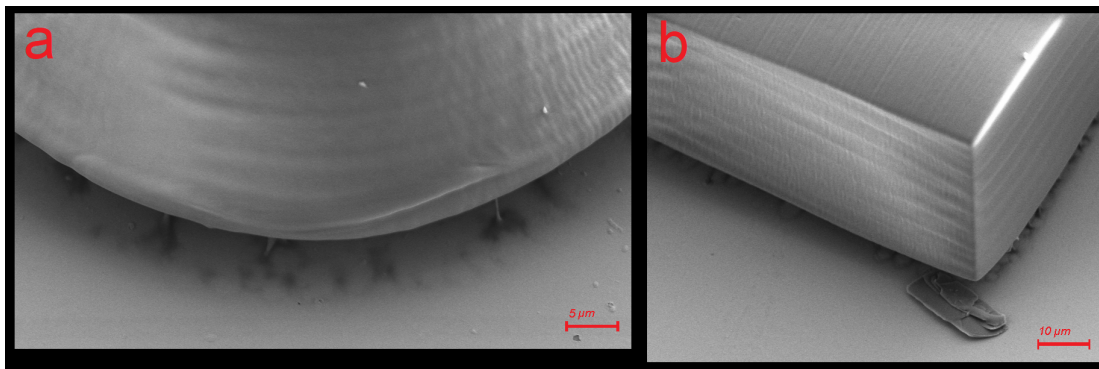
Figure 19 SEM images of prints showing liftoff from the substrate surface. **a)** The edge of a surface area print model of the type used to modify the electrode pads, scale bar 5 µm. **b)** the corner of a large box print, showing a significant gap between edge and substrate, scale bar 10 µm.

The impedance decrease observed for the electrode pads with no printed structure is consistent with expectations, as the surface area will be slightly increased by both the margin left inside the etching pattern as well as an increased roughness due to sputter coating. The lack of similar improvement in the pads with prints was found to be a result of a lack of electrical connection between the print surface and the electrode surface. If no electrical connection is formed to the structure during sputtering, then it will not increase available surface area but instead will decrease it as the structure covers a large portion of the electrode. The likely cause of this disconnect is the combination of prints intentionally placed at or slightly above the surface combined with the shrinking behavior of DLW polymers. During the printing process, DLW structures will exhibit shrinkage due to polymer cross-linking and thermal effects from cooling after laser polymerization (Li et al. 2008). This lift-off pattern was confirmed using SEM imaging, with a lift-off height of one or more microns (Figure 19). As
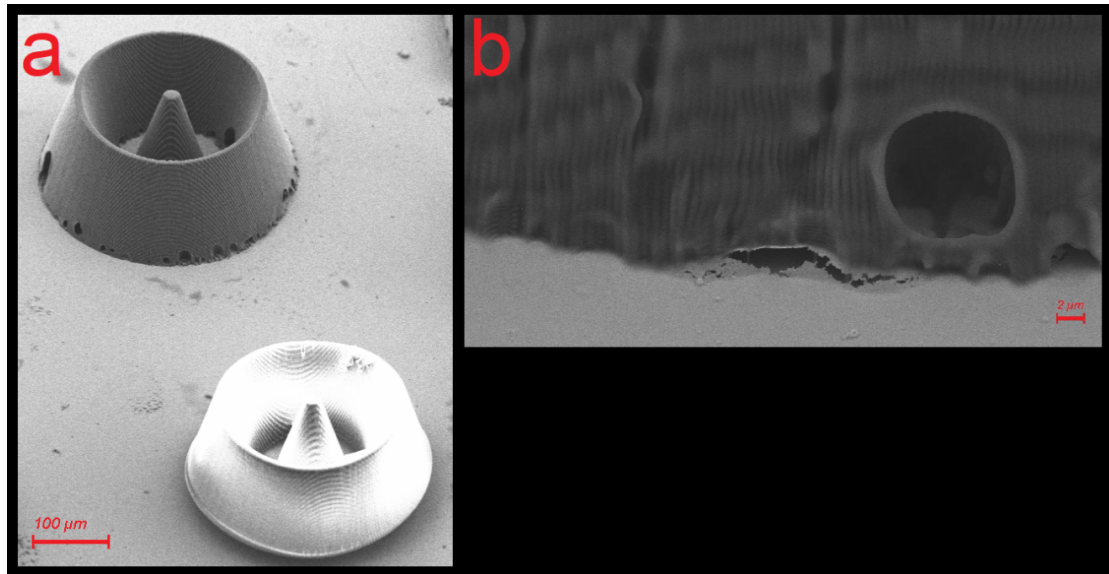
Figure 20 a) Two prints on 125 nm gold sputtered on silicon. Bottom print was printed slightly above the surface and shows significant liftoff. Whiteout effect on bottom print caused by electron buildup during SEM imaging, a result of lack of electrical connection to the surface. Upper print was printed slightly below the surface, and shows close attachment to surface as well as no SEM whiteout effect. Scale bar 100 µm. **b)** Closeup of top print in a, showing attachment to surface by 7 nm gold thin film used for SEM imaging, as well as minor dielectric breakdown distortions. Scale bar 2 µm.

thin films coatings were in the tens or hundreds of nanometers, these films would not be capable of bridging this gap.

In order to overcome this problem, we investigated an approach where prints were intentionally placed slightly lower than previous efforts, ~5 µm below the surface of the substrate. This produced a smooth connection to the surface of the electrodes. While some dielectric breakdown was still observed, it occurred at a small enough scale not to affect the electrical connection to the surface nor the overall structure of the prints, which remained attached to the substrate (Figure 20).
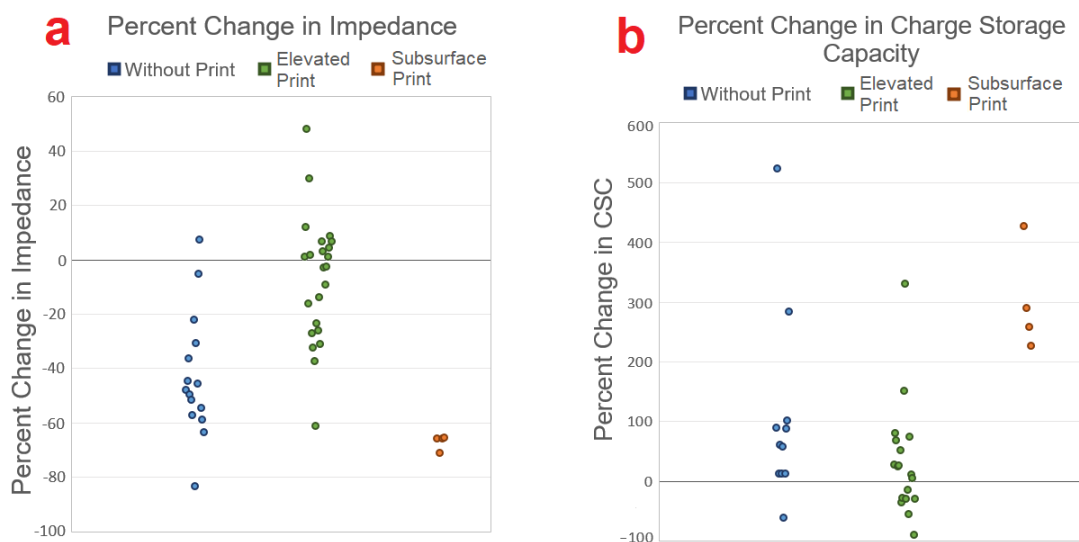
Figure 21 a) Percentage change in impedance for all pads without surface area increasing print (n = 15), original set of pads with above-substrate prints (n = 23), and pads with subsurface printing of structures for improved surface connection (n = 4). A more negative impedance change is indicative of a more effective electrode. **b)** Percentage change in charge storage capacity for all pads without surface area increasing print (n = 11), original set of pads with above-substrate prints (n = 18), and pads with subsurface printing of structures for improved surface connection (n = 4). A more positive CSC change is indicative of a more effective electrode.

This method was used to produce another set of measurements on 200 μm and 400 μm pads. Seven electrodes were used, four with subsurface prints and three without. The pads featuring a print showed a percent reduction in impedance which was significantly greater than the reduction seen in the pads without a print (p < 0.05) (Figure 21a). Improvements in charge storage capacity were also observed, however the difference between the pads with prints and those without did not reach significance (Figure 21b).

Though small in sample size, this positive result is an indicator of the viability of this method to reduce electrode impedance without changing footprint. The subsurface print data also shows a reduced variance, which may be an

indication of higher reliability using the subsurface printing method, or simply a result of the small number of data points collected thus far.

3.3 Process Limitations and Variations

3.3.1 Printing and Structure Design

While the driving design factor for the print structures used was maximizing coated surface area, a number of other limitations came into play as well. To properly optimize print shape, an extensive series of models and tests would be required examining shrinkage effects across different polymers and structures, voltage distribution across differently shaped electrode surfaces, and effectiveness of coating on angled surfaces for different metallization methods. Similar to pore resistance, it is possible that air bubbles may become trapped in recessed regions of printed structures, reducing their measured effectiveness significantly as electrolyte is blocked from the electrode surface. Given the circular design of the prints used in this study, this is a particular possibility and additional source of error.

Additional constraints must be factored in if printed structures are to be used as electrode modifications in vivo. This technology does offer the printing resolution to make direct fabrication of sub-10 µm electrodes possible, creating the opportunity to produce CNS implantable electrodes smaller than the immune response threshold. However, this will greatly increase challenges faced with regards to attachment strength and structural integrity given such small prints. In

theory, the sub-micron feature sizes which can be achieved using DLW printing combined with metallization coatings in the tens of nanometers should allow for the fabrication of complex high-surface area shapes while remaining within the sub-10 μm size range.

Structures could be fabricated using other polymers aside from IP-Dip, such as SU-8 or OrmoComp, which may provide parameters better suited for particular goals or fabrication methods such as optimization for higher resolutions in certain systems, reduced shrinkage, or different optical properties for lenses. There has also been some investigation into the use of metal-doped conductive polymers used for DLW printing (Nakamura et al. 2016), however this doping process can reduce structural integrity of prints as well as offering a lower conductivity than surface applied metal films. This opportunity for customization is both still a blind spot in the information available on this new metal printing fabrication method, as well as an encouraging scope of possibilities that may offer solutions to future problems that arise.

3.3.2 Metallization

Quantifying the success of the metallization process presented a challenge. As the gold film deposited is tens of nanometers thick and intended to render the full surface conductive, it cannot be easily examined under scanning electron microscope for many possible flaws such as too-thin coating. Additionally, the height of the prints presented potential shadowing complications which could prevent structures from being evenly coated if the angle of

deposition is imperfect.

Thin films deposited onto a substrate suffer from thermal stresses due to cooling-driven contraction after deposition. As the surface of the film is unconstrained but the base of the film is locked in position to the substrate, the difference in thermal expansion coefficients results in a stress being placed onto the film. Other intrinsic sources of differential volume change result in additional stresses as well (Liu 2012). For a high thickness thin film, this may result in cracking and delamination of the film from the surface.

Alternative deposition methods are possible that could produce a more reliably even coating. Chemical vapor deposition (CVD) is a commonly used method for the laying of metal material thin films evenly across a complexly shaped surface, as a nondirectional coating method. As it is less directional than sputtering, CVD could potentially also present a solution to the lift-off challenge without requiring subsurface printing. One common concern with CVD methods is the high temperature necessary for its use, which could cause damage to the polymer structures. IP-Dip polymer has been used to fabricate high precision structures even after baking at 690 C and remained structurally stable (Seniutinas et al. 2018), albeit with changes in chemical composition, suggesting that it may be suitable as a temperature resistant substrate for CVD coating.

3.3.3 Laser Etching of Sputtered Films

While the etching process was confirmed in thinner films to electrically isolate the pads from one another, it is possible that it introduced other

confounding elements. Etching-induced damage to the silicon carbide coated traces immediately surrounding the pads may have inadvertently increased surface area, though this increase would appear equally in without-print controls. As the fluorescein-dextran solution used for visualization was saline-based, it presented a different index of refraction than the lens used for etching which may have affected the focusing of the laser: while the etch process appeared to be successful, this may have introduced focusing problems with etch evenness that could complicate these results.

One set of electrodes was prepared using film of 150 nm thickness instead of the 30–40 nm used for other electrodes to see if this provided improvements in electrical connection between substrate and print. When exposed to the laser etching process, this thicker film cracked and folded without fully breaking apart and electrical shorts remained between the different pads even after the etching process was repeated several times (Figure 22). This suggests a limitation for thickness above which the laser etching process requires adjustment to be suitable for use. It may be possible to produce more reliable etching results with a laser designed for the purpose of etching, as opposed to a directly repurposed printing laser. For example, alternative approaches could present a higher pulse power. Alternatively, if a thick film is required, other gold film etching methods could be substituted such as masking with chemical etching, a well-established method for removal of thicker gold films (Liu 2012).
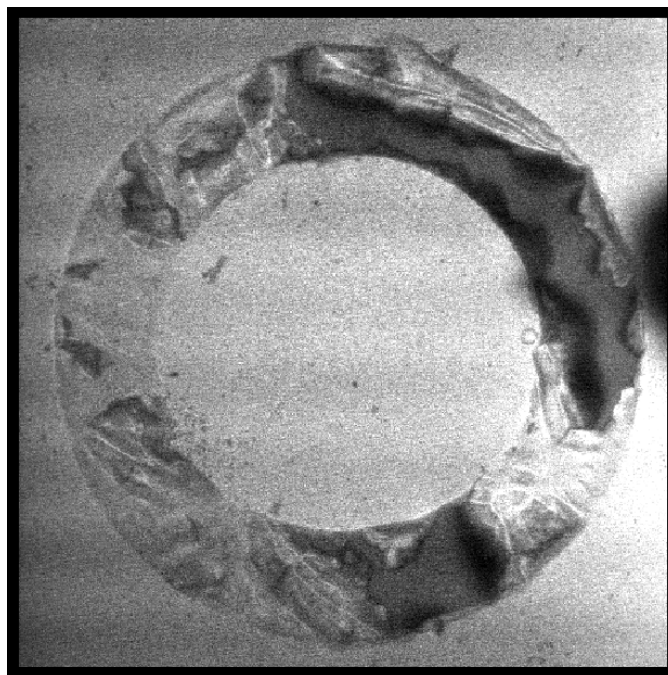
Figure 22 Visualization image taken using the rDLW printer system with fluorescein-dextran solution as fluorescent medium. Laser etching attempts on 150 nm gold thin film produced cracking and peeling rather than smooth removal of the film, leaving shorts behind that remained intact even after repeated etch processes directed at the same area.

3.3.4 Characterization

The characterization arrangement used produced quite repeatable results suggesting reliability, though this does not preclude persistent sources of error. Several patterns became highly apparent during characterization with regard to the effects of the characterization process on the parameters measured.

It is known that upon initial submersion in water-based liquids such as PBS these characterization measurements will shift initially over the first several minutes, as the liquid infiltrates cracks and details in the electrode surfaces. For this reason, we waited 15 minutes after submersion of the electrodes in PBS before beginning measurements. Two CV and three EIS measurements were

taken for each pad, in a consistent order across twelve pads. The results from the second set of CV and second and third set of EIS measurements reliably showed a lower impedance and a higher CSC than the first set. Cyclic Voltammetry cycles are capable of cleaning off some contaminants from an electrode surface (Elgrishi et al. 2017) and this process may explain the difference in values appearing before and after the first CV result, especially as impedance values appeared to stabilize after the first CV, between measurements 2 and 3. Use of a consistent characterization run order helped limit the impact of this effect.

3.4 Next Steps

The results presented here show the viability of this technique for use in fabrication of microdevices of a range of utility, with preliminary numerical validation for its application in electrode modification. This work opens the door to future experiments in optimizing and advancing rDLW based microfabrication.

The electrode improvement process might be further explored through the consideration of different potential print shapes to determine an optimal outcome across different polymers. Alternative means of coating such as CVD have the potential to greatly improve coverage and reliability of the metallization process. Likewise, a system designed with the intention of laser etching on highly reflective surfaces may provide much more suited parameters for that aspect of the process.

One of the primary next milestones to work towards is investigation of in

vivo use of modified electrodes. The additional constraints and challenges of the in vivo environment present one of the larger hurdles any newly proposed biomedical technology must overcome, and it is unknown whether this system will present previously undetected flaws when tested in this context.

The most important area to follow up on is the development of a better understanding of the printing on metal successes observed here. It would be extremely valuable to acquire better data regarding how different contexts make the dielectric breakdown phenomenon more or less severe. One of the first priorities in this pursuit would be to identify the origins of the success between DLW and rDLW systems, which will likely entail the creation of an adjustable speed rDLW printer system as the current primary theory behind the success.

4 Conclusion

This work presents a next step along a path towards efficient microstructure fabrication. While the combination of polymer and metal structures has long been used, it comes with extreme limitations in context and shape. Breakthroughs in complex shape fabrication from DLW printing have opened the floodgates for the rapid fabrication of physical microactuators, metamaterials, lenses, and other microstructure devices. Nonetheless, limitations remain. This research offers the possibility of overcoming one of those limitations: that of DLW fabrication directly onto reflective surfaces such as metals, and demonstrates one potential application of that technology through the fabrication and characterization of improved electrodes. The results found so far are promising as to the utility of this method in applied research in the near future.

5 References

Amon, A., and F. Alesch. "Systems for deep brain stimulation: review of technical features." Journal of Neural Transmission 124.9 (2017): 1083-1091.

Arroyo-Currás, Netzahualcóyotl, Karen Scida, Kyle L. Ploense, Tod E. Kippin, and Kevin W. Plaxco. "High Surface Area Electrodes Generated via Electrochemical Roughening Improve the Signaling of Electrochemical Aptamer-Based Biosensors." Analytical Chemistry 89.22 (2017): 12185–12191.

Atwater, J. H., et al. "Microphotonic parabolic light directors fabricated by two-photon lithography." Applied Physics Letters 99.15 (2011): 151113.

Beebe, Xenia, and T. L. Rose. "Charge injection limits of activated iridium oxide electrodes with 0.2 ms pulses in bicarbonate buffered saline (neurological stimulation application)." IEEE Transactions on Biomedical Engineering 35.6 (1988): 494-495.

Belazaras, Kastytis, et al. "Femtosecond laser polymerization of hybrid/integrated micro-optical elements and their characterization." Journal of Optics 12.124010 (2010): 124010.

Benninger, Richard KP, and David W. Piston. "Two-photon excitation microscopy for the study of living cells and tissues." Current Protocols in Cell Biology 59.1 (2013): 4-11.

Bhandari, Rajmohan, Sandeep Negi, and Florian Solzbacher. "Wafer-scale fabrication of penetrating neural microelectrode arrays." Biomedical Microdevices 12.5 (2010): 797-807.

Bhansali, Shekhar, and Abhay Vasudev, eds. MEMS for biomedical applications. Elsevier, 2012.

Biran, Roy, David C. Martin, and Patrick A. Tresco. "Neuronal cell loss accompanies the brain tissue response to chronically implanted silicon microelectrode arrays." Experimental Neurology 195.1 (2005): 115-126.

"Blackrock Microsystems Electrodes." Neuroscience Research Systems | Blackrock Microsystems, 2016, blackrockmicro.com/.

Brownlee, Robert R. "Pacemaker catheter utilizing bipolar electrodes spaced in accordance to the length of a heart depolarization signal." U.S. Patent No. 5,127,403. 7 Jul. 1992.

Brumberg, Jonathan S., et al. "Brain–computer interfaces for speech communication." Speech Communication 52.4 (2010): 367-379.

Burke, L. D., and P. F. Nugent. "The electrochemistry of gold: I the redox behaviour of the metal in aqueous media." Gold Bulletin 30.2 (1997): 43-53.

Butson, Christopher R., and Cameron C. McIntyre. "Role of electrode design on the volume of tissue activated during deep brain stimulation." Journal of Neural Engineering 3.1 (2005): 1.

Bückmann, Tiemo, et al. "Tailored 3D mechanical metamaterials made by dip-in direct-laser-writing optical lithography." Advanced Materials 24.20 (2012): 2710-2714.

Clark, Graeme M. "The multiple-channel cochlear implant: the interface between sound and the central nervous system for hearing, speech, and language in deaf people—a personal perspective." Philosophical Transactions of the Royal Society B: Biological Sciences 361.1469 (2006): 791-810.

Cogan, Stuart F. "Neural Stimulation and Recording Electrodes." Annual Review of Biomedical Engineering 10 (2008): 275–309.

Cogan, Stuart F., Julia Ehrlich, and Timothy D. Plante. 2014. "The Effect of Electrode Geometry on Electrochemical Properties Measured in Saline." Conference Proceedings: ... Annual International Conference of the IEEE Engineering in Medicine and Biology Society. IEEE Engineering in Medicine and Biology Society. Conference 2014: 6850–6853.

Cogan, S.F., Guzelian, A.A., Agnew, W.F., Yuen, T.G. and McCreery, D.B. "Over-pulsing degrades activated iridium oxide films used for intracortical neural stimulation." Journal of Neuroscience Methods 137.2 (2004): 141-150.

Cogan, Stuart F., et al. "In vitro comparison of the charge-injection limits of activated iridium oxide (AIROF) and platinum-iridium microelectrodes." IEEE Transactions on Biomedical Engineering 52.9 (2005): 1612-1614.

Cumpston, Brian H., et al. "Two-photon polymerization initiators for three-dimensional optical data storage and microfabrication." Nature 398.6722 (1999): 51.

Dalzell, Gavin WN, et al. "Electrode pad size, transthoracic impedance and success of external ventricular defibrillation." The American Journal of Cardiology 64.12 (1989): 741-744.

Deku, Felix, et al. "Electrodeposited iridium oxide on carbon fiber ultramicroelectrodes for neural recording and stimulation." Journal of The Electrochemical Society 165.9 (2018): D375-D380.

Deku, Felix, et al. "Amorphous silicon carbide ultramicroelectrode arrays for neural stimulation and recording." Journal of Neural Engineering 15.1 (2018): 016007.

Elgrishi, Noémie, et al. "A practical beginner's guide to cyclic voltammetry." Journal of Chemical Education 95.2 (2017): 197-206.

Fahraeus, T., C. W. Israel, and M. Wöllenstein. "Thin co-radial bipolar leads: technology and clinical performance." Herzschrittmachertherapie & Elektrophysiologie 12.3 (2001): 148-157.

Farsari, Maria, and Boris N. Chichkov. "Materials processing: Two-photon fabrication." Nature Photonics 3.8 (2009): 450.

Farsari, Maria, et al. "Two-photon polymerization of an Eosin Y-sensitized acrylate composite." Journal of Photochemistry and Photobiology A: Chemistry 181.1 (2006): 132-135.

Frank, K., and Mo GF Fuortes. "Potentials recorded from the spinal cord with microelectrodes." The Journal of Physiology 130.3 (1955): 625-654.

Gällentoft, Lina, Lina M. E. Pettersson, Nils Danielsen, Jens Schouenborg, Christelle N. Prinz, and Cecilia Eriksson Linsmeier. 2015. "Size-Dependent Long-Term Tissue Response to Biostable Nanowires in the Brain." Biomaterials 42 (2015): 172–183.

Gandiga, Prateek C., Friedhelm C. Hummel, and Leonardo G. Cohen. "Transcranial DC stimulation (tDCS): a tool for double-blind sham-controlled clinical studies in brain stimulation." Clinical Neurophysiology 117.4 (2006): 845-850.

Gansel, Justyna K., et al. "Gold helix photonic metamaterial as broadband circular polarizer." Science 325.5947 (2009): 1513-1515.

Geddes, L. A., and R. Roeder. "Criteria for the selection of materials for implanted electrodes." Annals of Biomedical Engineering 31.7 (2003): 879-890.

Gissibl, Timo, et al. "Two-photon direct laser writing of ultracompact multi-lens objectives." Nature Photonics 10.8 (2016): 554.

Gottmann, Jens, et al. "High speed and high precision fs-laser writing using a scanner with large numerical aperture." Journal of Laser Micro/ Nanoengineering 4.3 (2009): 192-196.

Green, Rylie A., et al. "Conducting polymers for neural interfaces: challenges in developing an effective long-term implant." Biomaterials 29.24-25 (2008): 3393-3399.

Guitchounts, Grigori, et al. "A carbon-fiber electrode array for long-term neural recording." Journal of Neural Engineering 10.4 (2013): 046016.

Hallett, Mark. "Transcranial magnetic stimulation and the human brain." Nature 406.6792 (2000): 147.

Harris, Alexander R., Carrie Newbold, Paul Carter, Robert Cowan, and Gordon G. Wallace. 2018. "Measuring the Effective Area and Charge Density of Platinum Electrodes for Bionic Devices." Journal of Neural Engineering 15.4 (2018): 046015.

Heuschkel, Marc O. 2001. Fabrication of Multi-Electrode Array Devices for Electrophysiological Monitoring of In-Vitro Cell/tissue Cultures. Thesis – Ecole polytechnique federale de Lausanne (EPFL). doi: 10.5075/epfl-thesis-2370

Jones, Kelly E., Patrick K. Campbell, and Richard A. Normann. "A glass/silicon composite intracortical electrode array." Annals of Biomedical Engineering 20.4 (1992): 423-437.

Joye, Neil, Alexandre Schmid, and Yusuf Leblebici. "Electrical Modeling of the Cell–electrode Interface for Recording Neural Activity from High-Density Microelectrode Arrays." Neurocomputing 73.1-3 (2009): 250–259.

Jun, James J., et al. "Fully integrated silicon probes for high-density recording of neural activity." Nature 551.7679 (2017): 232.

Kawata, Satoshi, et al. "Finer features for functional microdevices." Nature 412.6848 (2001): 697.

Kellis, Spencer S., et al. "Human neocortical electrical activity recorded on nonpenetrating microwire arrays: applicability for neuroprostheses." Neurosurgical Focus 27.1 (2009): E9.

Kim, Seung-Jae, et al. "Electrophysiological mapping of cat primary auditory cortex with multielectrode arrays." Annals of Biomedical Engineering 34.2 (2006): 300-309.

Kipke, Daryl R., et al. "Silicon-substrate intracortical microelectrode arrays for long-term recording of neuronal spike activity in cerebral cortex." IEEE Transactions on Neural Systems and Rehabilitation Engineering 11.2 (2003): 151-155.

Kummamuru, Ravi K., Liang Hu, Lawrence Cook, Mikhail Y. Efremov, Eric A. Olson, and Leslie H. Allen. "A Close Proximity Self-Aligned Shadow Mask for Sputter Deposition onto a Membrane or Cavity." *Journal of Micromechanics and Microengineering: Structures, Devices, and Systems* 18.9 (2008): 095027.

Lempka, Scott F., et al. "Optimization of microelectrode design for cortical recording based on thermal noise considerations." 2006 International Conference of the IEEE Engineering in Medicine and Biology Society. IEEE, 2006.

Li, Yan, et al. "Nonuniform shrinkage and stretching of polymerized nanostructures fabricated by two-photon photopolymerization." Nanotechnology 19.5 (2008): 055303.

Li, Yue, and David J. Mogul. "Electrical control of epileptic seizures." Journal of Clinical Neurophysiology 24.2 (2007): 197-204.

Lissandrello, Charles A., et al. "A micro-scale printable nanoclip for electrical stimulation and recording in small nerves." Journal of Neural Engineering 14.3 (2017): 036006.

Liu, Chang. Foundations of MEMS. Pearson Education India, 2012.

Lykken, David T., and Peter H. Venables. "Direct measurement of skin conductance: A proposal for standardization." Psychophysiology 8.5 (1971): 656-672.

Maruo, Shoji, and Koji Ikuta. "Three-dimensional microfabrication by use of single-photon-absorbed polymerization." Applied Physics Letters 76.19 (2000): 2656-2658.

Maruo, Shoji, Osamu Nakamura, and Satoshi Kawata. "Three-dimensional microfabrication with two-photon-absorbed photopolymerization." Optics Letters 22.2 (1997): 132-134.

Maynard, Edwin M., Craig T. Nordhausen, and Richard A. Normann. "The Utah intracortical electrode array: a recording structure for potential brain-computer interfaces." Electroencephalography and Clinical Neurophysiology 102.3 (1997): 228-239.

Merrill, Daniel R., Marom Bikson, and John GR Jefferys. "Electrical stimulation of excitable tissue: design of efficacious and safe protocols." Journal of Neuroscience Methods 141.2 (2005): 171-198.

Micera, Silvestro, and Xavier Navarro. "Bidirectional interfaces with the peripheral nervous system." International Review of Neurobiology 86 (2009): 23-38.

Miller, C. G., L. Cornish, C. Jones, C. G. Jones, and A. S. Henderson. "A New Laser Method for Cleaning Micropalaeontological Specimens." Journal of Micropalaeontology 23.2 (2004): 165–169.

Mirvis, David M., and Ary L. Goldberger. "Electrocardiography." Heart Disease 1 (2001): 82-128.

Moss, J., et al. "Electron microscopy of tissue adherent to explanted electrodes in dystonia and Parkinson's disease." Brain 127.12 (2004): 2755-2763.

Mushahwar, Vivian K., David F. Collins, and Arthur Prochazka. "Spinal cord microstimulation generates functional limb movements in chronically implanted cats." Experimental Neurology 163.2 (2000): 422-429.

Nadol Jr, Joseph B., et al. "Cellular immunologic responses to cochlear implantation in the human." Hearing Research 318 (2014): 11-17.

Nakamura, Ryotaro, et al. "Fabrication of gold microstructures using negative photoresists doped with gold ions through two-photon excitation." Physical Chemistry Chemical Physics 18.25 (2016): 17024-17028.

Negi, Sandeep, et al. "Neural electrode degradation from continuous electrical stimulation: comparison of sputtered and activated iridium oxide." Journal of Neuroscience Methods 186.1 (2010): 8-17.

Niesler, Fabian, and Yann Tanguy. "3D Printers for the Fabrication of Micro-Optical Elements: Disruptive technology enables the way for unprecedented applications." Optik & Photonik 11.4 (2016): 44-47.

Obata, Kotaro, et al. "High-aspect 3D two-photon polymerization structuring with widened objective working range (WOW-2PP)." Light: Science & Applications 2.12 (2013): e116.

Patel, Paras R., et al. "Insertion of linear 8.4 μm diameter 16 channel carbon fiber electrode arrays for single unit recordings." Journal of Neural Engineering 12.4 (2015): 046009.

Pearce, J. A., et al. "Skin burns from electrosurgical current." Medical Instrumentation 17.3 (1983): 225-231.

Pearre, Benjamin W., Christos Michas, Jean-Marc Tsang, Timothy J. Gardner, and Timothy M. Otchy. 2018. "Fast micron-scale 3D printing with a resonant-scanning two-photon microscope." *arXiv Preprint* 1803 (07135). https://arxiv.org/abs/1803.07135.

Pistohl, Tobias, et al. "Prediction of arm movement trajectories from ECoG-recordings in humans." Journal of Neuroscience Methods 167.1 (2008): 105-114.

Polikov, Vadim S., Patrick A. Tresco, and William M. Reichert. "Response of brain tissue to chronically implanted neural electrodes." Journal of Neuroscience Methods 148.1 (2005): 1–18.

Posey, F. A., and T. Morozumi. "Theory of potentiostatic and galvanostatic charging of the double layer in porous electrodes." Journal of the Electrochemical Society 113.2 (1966): 176-184.

Pranti, Anmona S., et al. "Highly stable PEDOT: PSS coating on gold microelectrodes with improved charge injection capacity for chronic neural stimulation." Multidisciplinary Digital Publishing Institute Proceedings. Vol. 1. No. 4. 2017.

Rijkhoff, Nico JM, et al. "Selective stimulation of sacral nerve roots for bladder control: a study by computer modeling." IEEE Transactions on Biomedical Engineering 41.5 (1994): 413-424.

Rill, Michael S., et al. "Photonic metamaterials by direct laser writing and silver chemical vapour deposition." Nature Materials 7.7 (2008): 543.

Rekštytė, S., T. Jonavičius, and M. Malinauskas. "Direct laser writing of microstructures on optically opaque and reflective surfaces." Optics and Lasers in Engineering 53 (2014): 90-97.

Robblee, L. S. "Activated Ir: An electrode suitable for reversible charge injection in saline solution." Journal of the Electrochemical Society 130.3 (1983): 731.

Robblee, L. S., et al. "Electrical stimulation with Pt electrodes. VII. Dissolution of Pt electrodes during electrical stimulation of the cat cerebral cortex." Journal of Neuroscience Methods 9.4 (1983): 301-308.

Rohde, Charles A., Hayley Ware, Fraser MacMillan, Malkhaz Meladze, and M. Cather Simpson. "Selective gold film removal from multi-layer substrates with nanosecond UV pulsed laser ablation." Applied Physics A: Materials Science & Processing 111.2 (2013): 531–537.

Rubehn, Birthe, et al. "A MEMS-based flexible multichannel ECoG-electrode array." Journal of Neural Engineering 6.3 (2009): 036003.

Salatino, Joseph W., Kip A. Ludwig, Takashi D. Y. Kozai, and Erin K. Purcell. "Glial Responses to Implanted Electrodes in the Brain." Nature Biomedical Engineering 1.11 (2017): 862–877.

Sekirnjak, Chris, Pawel Hottowy, Alexander Sher, Wladyslaw Dabrowski, Alan M. Litke, and E. J. Chichilnisky. "High-Resolution Electrical Stimulation of Primate Retina for Epiretinal Implant Design." Journal of Neuroscience 28.17 (2008): 4446–4456.

Selimis, Alexandros, Vladimir Mironov, and Maria Farsari. "Direct laser writing: Principles and materials for scaffold 3D printing." Microelectronic Engineering 132 (2015): 83-89.

Seniutinas, G., et al. "Beyond 100 nm resolution in 3D laser lithography—Post processing solutions." Microelectronic Engineering 191 (2018): 25-31.

Skylar-Scott, Mark A., et al. "Multi-photon microfabrication of three-dimensional capillary-scale vascular networks." Advanced Fabrication Technologies for Micro/Nano Optics and Photonics X. Vol. 10115. International Society for Optics and Photonics, 2017.

Straka, Malgorzata, et al. "Characterizing Longitudinal Changes in the Impedance Spectra of In-Vivo Peripheral Nerve Electrodes." Micromachines 9.11 (2018): 587.

Sun, Hong-Bo, and Satoshi Kawata. "Two-photon photopolymerization and 3D lithographic microfabrication." NMR• 3D Analysis• Photopolymerization. Springer, Berlin, Heidelberg, 2004. 169-273.

Szarowski, D. H., et al. "Brain responses to micro-machined silicon devices." Brain Research 983.1-2 (2003): 23-35.

Tanaka, Takuo, Atsushi Ishikawa, and Satoshi Kawata. "Two-photon-induced reduction of metal ions for fabricating three-dimensional electrically conductive metallic microstructure." Applied Physics Letters 88.8 (2006): 081107.

Tien, Lee W., et al. "Silk as a multifunctional biomaterial substrate for reduced glial scarring around brain-penetrating electrodes." Advanced Functional Materials 23.25 (2013): 3185-3193.

Veraart, Claude, et al. "Pattern recognition with the optic nerve visual prosthesis." Artificial Organs 27.11 (2003): 996-1004.

Vitale, Flavia, et al. "Neural stimulation and recording with bidirectional, soft carbon nanotube fiber microelectrodes." ACS Nano 9.4 (2015): 4465-4474.

Weiland, James D., David J. Anderson, and Mark S. Humayun. "In vitro electrical properties for iridium oxide versus titanium nitride stimulating electrodes." IEEE Transactions on Biomedical Engineering 49.12 (2002): 1574-1579.

Wise, Kensall D., James B. Angell, and Arnold Starr. "An integrated-circuit approach to extracellular microelectrodes." IEEE Transactions on Biomedical Engineering 3 (1970): 238-247.

Yoon, Inho, et al. "Intracellular neural recording with pure carbon nanotube probes." PLoS One 8.6 (2013): e65715.

Zhong, Yinghui, and Ravi V. Bellamkonda. "Controlled release of anti-inflammatory agent α-MSH from neural implants." Journal of Controlled Release 106.3 (2005): 309-318.

Žukauskas, Albertas, et al. "Black silicon: Substrate for laser 3D micro/nano-polymerization." Optics Express 21.6 (2013): 6901-6909.

Zychowicz, Tomasz, Jerzy Krupka, and Janina Mazierska. 2006. "Measurements of Conductivity of Thin Gold Films at Microwave Frequencies Employing Resonant Techniques." In 2006 Asia-Pacific Microwave Conference.

CURRICULUM VITAE